J.M. Reynolds-Barredo, et al. Effect of non axisymmetric perturbations on the ambipolar $E_r$ and neoclassical particle flux inside the ITER pedestal region, In: *Nuclear fusion, 60(8), 086017, 21 pp.*

DOI: https://doi.org/10.1088/1741-4326/ab992e

# Effect of non axisymmetric perturbations on the ambipolar $E_r$ and neoclassical particle flux inside the ITER pedestal region

**J. M. Reynolds-Barredo[1], V. Tribaldos[1], A. Loarte[2], A.R. Polevoi[2], M. Hosokawa[2] and R. Sanchez[1]**

[1] Departamento de Física, Universidad Carlos III de Madrid, Leganés 28911, Spain
[2] ITER Organization, Route de Vinon-sur-Verdon, 13067 St Paul Lez Durance, France

**Abstract.**

The transport dynamics of impurities in the pedestal region of ITER plasmas is of crucial interest since this regulates the penetration of impurities from the edge into the core plasma, where an excessive accumulation of impurities can degrade their fusion performance. In the pedestal region of H-mode tokamak plasmas anomalous transport is highly reduced and impurity transport is found to be well described by neoclassical theory. Under these conditions, perturbations to the axisymmetric tokamak geometry can strongly affect both radial electric field and particle transport. In this work, we describe the results of numerical studies performed to quantify the effects on the pedestal ambipolar electric field and radial particle fluxes of the non-axisymmetric fields, associated with both the intrinsic toroidal field ripple and extrinsic fields applied for ELM control, for ITER $Q = 10$ plasma conditions with emphasis on high Z impurity transport. It is found that the effect of the ITER toroidal field ripple on high Z impurity transport is negligible. On the contrary, extrinsic three-dimensional fields applied for ELM control cause a strong modification of the pedestal ambipolar electric (to less negative values) and the appearance of multi-valued solutions for the pedestal electric field, analogue to core stellarator transport significantly increasing the outward character of neoclassical pedestal transport for both the main plasma ions (D and T in ITER) and high Z impurities, suggesting a strong modification of the background plasma profiles. Finally, it is found that, for the Z impurity, its quantitative evaluation has uncertainties (with important implications for the radial flow direction) associated with the high poloidal Mach number $\sim 1$, due to the high pedestal electric field and large ion mass, which renders first order neoclassical theory questionable. Detailed ITER MHD 3-D equilibria and a benchmark of SFINCS against NEO and NCLASS codes has also been obtained.

*Keywords*: ITER, impurity transport, ambipolar electric field, ripple, RMP coils, SFINCS

Submitted to: *Nuclear Fusion*

## 1. Introduction

ITER divertor materials are designed to handle large stationary and transient power fluxes for which high atomic charge metallic materials are best suited, when tritium retention considerations are taken into account. Even minute concentrations of these highly ionized high atomic number elements can decrease significantly fusion power production because of radiation losses (line radiation and Bremsstrahlung). Thus, to achieve its fusion performance objectives, ITER needs to minimize the inward transport of impurities from the plasma facing components, in particular the tungsten-armoured divertor, to avoid large power losses by radiation. To achieve the plasma performance required, ITER should operate in the H-mode regime and thus with an edge region with low plasma transport called the pedestal. Since the pedestal is the interface between the confined core plasma and the scrape-off layer, understanding the particle flux dynamics of the impurities in the pedestal region is of great importance for ITER.

There is an extensive literature studying the MHD equilibrium and stability [1] of the pedestal region against density and temperature gradients of different species and the transport of bulk ions and heavy impurities across it [2]. In these studies, tokamak configurations have been described considering the plasma toroidally symmetric, which is a fair approximation being used for the last forty years in this type of physics studies [3]. Despite this, tokamaks are not axisymmetric in practice. For instance, as many other tokamaks ITER contains some elements in its design that break magnetic field symmetry such as: i) the finite number of toroidal field coils (this is common to all tokamaks) and ferromagnetic inserts to reduce the non-axisymmetry of the toroidal field [4], ii) the 3-D fields created by the in-vessel ELM control coils, designed to suppress edge localized unstable modes (ELM) [5], iii) the Test Blanket Modules (TBMs) [6], which contain ferromagnetic steel, and will be used for demonstration of tritium production and iv) the magnetic field reduction systems [7] for the massive neutral beam injectors (NBI) to ensure a sufficiently low field in their interior. Though, these three-dimensional magnetic fields should not affect the ITER plasma core, they can significantly influence the stability of the pedestal, plasma-wall interaction localization and the impurity transport dynamics [2]. The study presented in this paper is focused on the consequences of breaking of the toroidal symmetry of ITER H-mode plasmas on impurity transport in the pedestal region of ITER H-mode plasmas. In particular we consider the effect of toroidal field ripple, due to the finite number of toroidal field coils and the effect of 3-D fields applied for ELM control, so-called RMP fields.

Inside the pedestal region of H-mode plasmas, anomalous transport is highly reduced. In particular, for impurities this reduction makes their transport to be described by the neoclassical approximation, as verified experimentally [8]. This stationary transport may be interrupted by MHD instabilities such as ELMs, which should be mitigated or suppress for ITER high Q operation [5]. Thus, the resulting impurity pedestal profile arises from a delicate equilibrium between influxes and outfluxes. In this paper we study the neoclassical contributions to these fluxes and,

in particular we investigate if non-axisymmetric deviations of the tokamak plasma equilibrium can affect the inward flux of tungsten, which is the dominant heavy element on ITER's plasma facing components.

Special attention deserves the radial electric field $E_r$ because of its influence on the impurity flux: in neoclassical theory, the particle flux of impurities is mainly controlled by the sign and magnitude of $E_r$. In fact, experiments show a strong correlation between RMP fields and the $E_r$ in the pedestal region [9]. We obtain the value of the radial electric field from the ambipolar condition of radial particle fluxes calculated including 3D effects on neoclassical transport, for whose evaluation we utilize equilibria with nested closed surfaces. This excludes the effect of magnetic islands or peripheral ergodic regions, which are observed when RMP fields are applied for ELM control [10, 11]. Since ergodic regions only occur in the very outer layers of the confined plasma, well away from the pedestal top, and a similar picture is expected for ITER when appropriate screening is included [12] we do not expect our limitation in the modelling of these layers to have a significant impact on the results presented in this paper. In this approximation, the non-axi-symmetric perturbations to the tokamak equilibria allow the apparition of different solutions for the ambipolar $E_r$ (roots). We thus study the effects of the real 3-D tokamak plasma geometry on the electric field and impurity transport by applying the neoclassical theory with the maximum possible detail, but keeping out the stochasticity effects on the magnetic topology.

Our study is divided in two steps:

- We first calculate the 3D MHD equilibrium corresponding to the non axisymmetric tokamak configuration under study using the numerical tools developed in the stellarator community. Specifically, the free boundary version of the VMEC code [13, 14, 15] is used.
- Then, we calculate the impurity particle flux (tungsten in our case) using neoclassical theory for the 3D magnetic field configurations equilibria obtained on the first step. The radial particle and energy transport can be readily obtained on toroidally symmetric devices using the axisymmetric limit of neoclassical theory [16, 17]. For the cases where the axisymmetry is strongly broken, stellarator mono-energetic techniques [18] can be used. However, in the cases that will be studied for ITER, where the breaking of the axisymmetry is small, monoenergetic techniques cannot easily guarantee the level of parallel momentum conservation required to describe almost quasi-axisymmetric systems [19, 20]. Fortunately, there are some neoclassical codes that can simultaneously handle complex geometries and still have the conservation properties required to recover the correct particle flux levels for quasy-symmetric plasma equilibria. In particular, we have chosen for this work SFINCS, a recently developed code [21, 22] that has been successfully applied to study the transport in stellarators [23] and tokamaks, including the effect of the toroidal field ripple on the toroidal rotation of ITER [24].

The manuscript is organized as follows. After describing the ITER scenarios of

interest (Sec. 2), the first step of the analysis will consist on generating realistic MHD equilibria for the different non-axisymmetric geometries of study (Sec. 3). We then perform benchmarks of the calculated particle fluxes with SFINCS against other codes and with respect to the monoenergetic coefficient approach (Secs. 4.1– 4.2) both for 2-D and 3-D configurations. In these benchmarks we identify important assumptions of the various modelling approaches and the limits of the approximations. The main topic of our studies is then described: the effect of the toroidal field ripple (Sec. 5) and RMP fields (Sec. 6) on the pedestal radial electric field and tungsten transport. Finally, we will discuss the main conclusions of the work on Sec. 7.

## 2. ITER scenario description

### *2.1. Plasma parameters and profiles*

The basic operational scenarios of ITER [25] include different regimes of gain ($Q$), plasma current ($I_p$) and toroidal field ($B_t$) among other parameters. Here, we will focus on the so called baseline scenario for inductive operation, which targets fusion gain $Q \approx 10$ and $I_p = 15$MA plasma current, with a toroidal field of $B_t = 5.3$T. The Mach number for toroidal plasma rotation in ITER is modelled to be low despite the sizeable rotation frequency [12], since the plasma temperature is very high. Thus, toroidal rotation is not considered in our equilibrium nor neoclassical transport modelling. We utilize the total pressure, $q$-factor and toroidal current radial profiles from the 2-D equilibrium to obtain the 3-D MHD equilibrium. Additionally, for our modelling of neoclassical transport the density and temperature radial profiles associated with each species are obtained from ITER integrated plasma simulations consistent with the 2-D equilibrium [26, 27]. These simulations include neoclassical and anomalous transport modelling of the core plasma and models for edge-core integration through MHD scalings for the pedestal pressure and boundary conditions for the separatrix density obtained with SOLPS simulations.

Additionally, for neoclassical transport the density and temperature radial profiles associated with each species are obtained from ITER integrated plasma simulations consistent with the 2-D equilibrium [26]. Along the paper, we will use the radial coordinate definitions:

$$x = \sqrt{\frac{\psi}{\psi_{max}}} \tag{1}$$

and

$$\hat{r} = \hat{a}x \tag{2}$$

where $\psi$ is the toroidal magnetic flux associated with a particular magnetic flux surface, $\psi_{max}$ is the toroidal magnetic flux at the last closed magnetic flux surface (LCFS) and $\hat{a}$ is the average radius at the LCFS. The pressure, $q$-factor, density and temperature profiles corresponding to the reference scenario used on this work are represented in

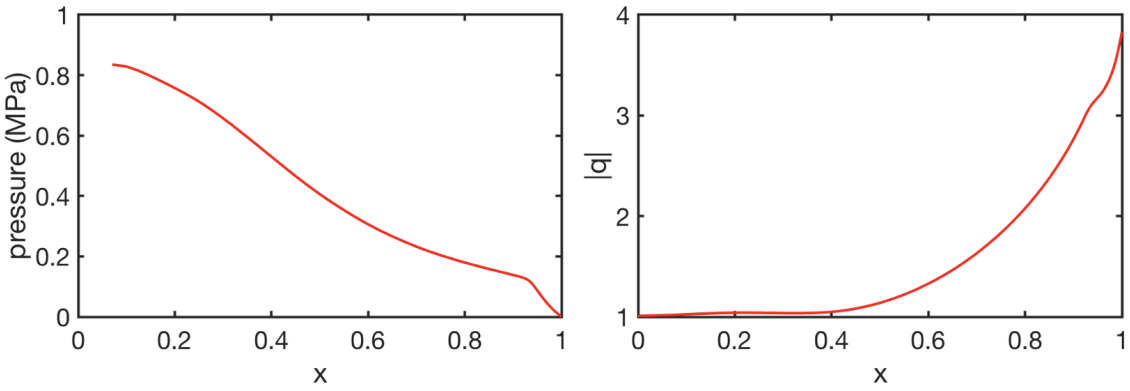


**Figure 1.** Pressure (left) and absolute value of the $q$-factor (right) profiles corresponding to the ITER reference scenario.

Fig. 1 and Fig. 2. The plasma is a mix of 50% deuterium and 50% tritium. The pressure profile includes the contributions of the suprathermal deuterons from NBI and alpha particles. Since for the cases under study we are interested in tungsten transport with fixed plasma profiles its density has been set to $10^{-6}$ times the density of the main species to ensure that the presence of tungsten would not affect the background plasma in ITER. The charge for the impurities has been chosen $Z_W = 20$; this represents a lower limit for the W ionization charge across the ITER pedestal region where the temperature covers the range of 0.2 - 5. keV [28]. The choice of a lower limit for $Z_W$ will be understood from the results in later sections.

### *2.2. Coils geometry and currents*

In order to calculate the MHD equilibrium, the real geometry and current of the 18 toroidal (TF), 6 poloidal (PF1 to PF6), 6 central solenoid modules (CS-1 to CS-6) and 27 ELM control coils that generate Resonant Magnetic Perturbation (RMP) fields (three toroidal row sets LOWER_ELM_01-09, MIDDLE_ELM_01-09, UPPER_ELM_01-09), were considered in our model. Every coil is modeled with several filaments to accurately take into account the complex cross section of the different components [29]. Details about the number of filaments and currents are given in Table 1, where $\phi_i$ represents the angular position of the centre of each ELM control coil and the different angle offsets $\phi_U$, $\phi_M$ and $\phi_L$ can be freely chosen for each ELM control coils set, e.g. to maximize the magnetic field perturbation close to the LCFS. For the poloidal and central solenoid coils a positive values implies currents flowing in the counter-clockwise direction as seen from the top, thus producing a magnetic field in positive Z direction. As for the toroidal coils, positive currents generate a toroidal magnetic field in the counter-clockwise direction as seen from above. Finally, positive currents in the ELM control coils generate a magnetic field pointing out of the plasma. As an example, the geometry of the filaments associated with the RMP coil descriptions is represented on Fig 3. For the studied scenario, both toroidal magnetic field and toroidal current of the

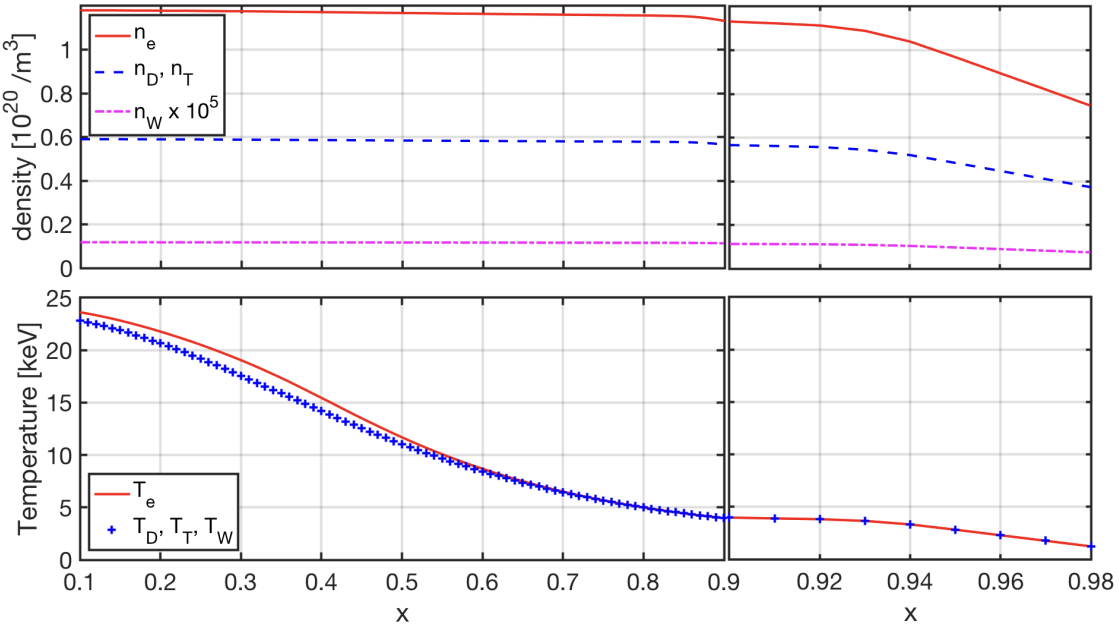


**Figure 2.** Density (top) and temperature (bottom) profiles corresponding to the ITER reference scenario. The radial range is split in the ranges $x = [0, 0.9]$ (left) and the region of the pedestal that will be analyzed in detail in this paper $x = [0.9, 0.98]$ (right).

ITER coils are on the clockwise direction (as seen from above); this is the reference for ITER to facilitate access to H-mode conditions with the minimum additional heating requirements (ion grad-B towards the divertor). In the coordinate system chosen in our studies (VMEC coordinates, with toroidal angle coincident with the cylindrical one), the toroidal magnetic flux is negative and the poloidal magnetic flux is positive. Thus, strictly speaking, the safety factor is negative, see Fig. 1 .

## 3. MHD equilibrium

Calculating the neoclassical transport in a particular configuration requires a precise knowledge of the magnetic geometry. Thus, the first step will be to construct the magnetic equilibria associated with the particular ITER scenario of interest. Along this work, nested magnetic surfaces in the studied volume, including the pedestal region will be assumed. This excludes the effect of magnetic islands or ergodic regions, which has been suggested as a possible mechanism of ELM mitigation/suppression due to the effect of RMP fields [30]. The reason for excluding this effect is purely practical: the tools for calculating the equilibrium and neoclassical transport with islands and ergodic regions are still not mature. Under such simplified magnetic geometry, one of the most used codes in the plasma community for calculating free boundary 3D MHD equilibrium is the VMEC code [13, 14, 15]. VMEC solves the MHD ideal equilibrium equation through a variational method using finite differences in the radial direction and

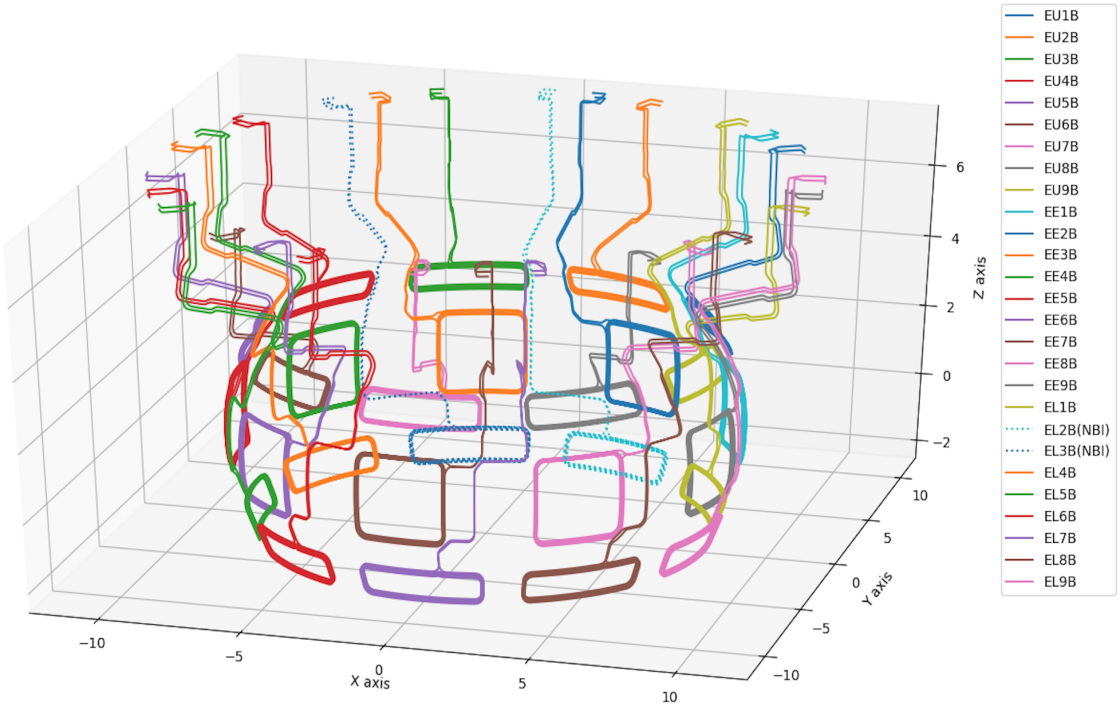


**Figure 3.** RMP coils detail. Distances in m.

| Coil description | filaments | current per filament (A) |
|---|---|---|
| CS3U | 553 | 1032.3 |
| CS2U | 553 | −51.0 |
| CS1U | 553 | 28383.4 |
| CS1L | 553 | 28383.6 |
| CS2L | 553 | 16626.8 |
| CS3L | 553 | −21202.5 |
| PF1 | 256 | −27351.6 |
| PF2 | 110 | 27930.9 |
| PF3 | 192 | 28734.9 |
| PF4 | 176 | 24158.0 |
| PF5 | 208 | 43946.2 |
| PF6 | 432 | −47194.4 |
| TF | 134 | −68119.0 |
| LOWER_ELM_0i | 6 | $15000.0\cos(\phi_i - \phi_L)$ |
| MIDDLE_ELM_0i | 6 | $15000.0\cos(\phi_i - \phi_M)$ |
| UPPER_ELM_0i | 6 | $15000.0\cos(\phi_i - \phi_U)$ |

**Table 1.** Currents associated with each coil.

a compact spectral decomposition in the angular dimensions. Along with the pressure

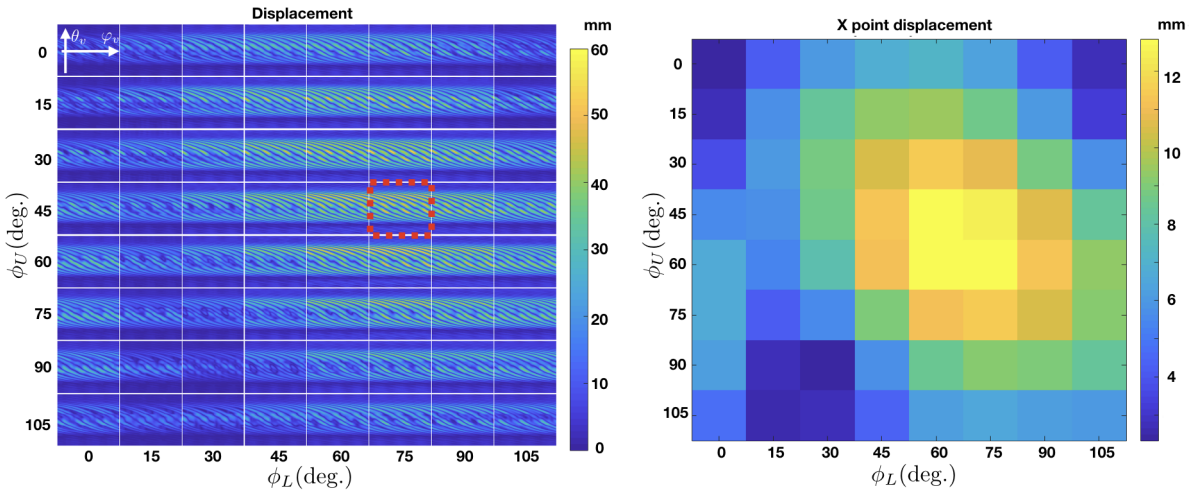


**Figure 4.** Left: Local distance between the unperturbed last magnetic surface for the $\mathbf{B}_{\rm AXI}$ and $\mathbf{B}_{RMP}$ equilibria for a scan in the RMP current angles $\phi_U$ and $\phi_L$ in VMEC coordinates $\theta_v$ and $\varphi_v$. Highlighted in red, the case chosen for this study $\phi_U = 45^o$, $\phi_L = 75^o$. Right: Same scan for the region around the X point.

profile, the free boundary version of VMEC also requires the full vacuum magnetic field in a regular grid for each reference scenario of Sec. 2. The equilibria used through this work can be group into three types, $\mathbf{B}_{\rm AXI}$, $\mathbf{B}_{\rm ripple}$ and $\mathbf{B}_{\rm RMP}$ depending on the symmetry of the magnetic field and the set of coils responsible of breaking it:

- $\mathbf{B}_{\rm AXI}$: Is the equilibrium solution of the MHD equations when the discrete nature of the TF coils is ignored, resulting in a torodially axisymmetric field. It will be used as a reference and as an intermediate check when compared with Grad-Shafranov solution.
- $\mathbf{B}_{\rm ripple}$: A set of five equilibria with toroidal magnetic field ripples ranging from 0.25% to 2% will be considered. These equilibria will be used for a sensitivity study of transport with ripple. Note that ITER toroidal field ripple at the outer separatrix midplane for 5.3 T is expected to be 0.3% thanks to the use of ferromagnetic inserts [4], while without them it would be 1.0% .
- $\mathbf{B}_{RMP}$: The effect of the RMP fields will be studied considering an equilibrium with the maximum nominal RELM control coil currents, 90kAturn [31] with $n = 3$ symmetry, and neglecting the toroidal ripple. The left plot in Fig. 4 shows the local distance between the unperturbed last magnetic surface, $\mathbf{B}_{\rm AXI}$, and its equivalent, $\mathbf{B}_{RMP}$, for a scan in the RMP current angles $\phi_U$ and $\phi_L$. The particular equilibrium chosen for this study $\mathbf{B}_{RMP}$ corresponding with $\phi_U = 45^o$ and $\phi_L = 75^o$ appears highlighted in the figure. This particular case shows large displacements that could potentially modify the neoclassical transport on the pedestal region. Finally, the maximum displacement around the X-point, see right plot in Fig. 4, is in good qualitative agreement with MARS-F simulations [30].

Note that the effects of the toroidal ripple and the RMP fields are treated separately. As will be shown in the next sections, the effect of toroidal ripple on pedestal neoclassical impurity transport is relatively small so that a realistic case including both effects together (ripple and RMP fields) is not expected to show qualitative differences to studying then separately. Thus we will consider both effects in separates studies. Moreover, the combined effects of both types of fields reduces the symmetry of the problem (from 18 or 3 periods to only one for the whole three-dimensional tokamak plasma) and significantly increases the computational cost of the simulations because of the higher toroidal resolution required.

The numerical accuracy of the solutions to the ideal MHD equations obtained with the VMEC code were checked increasing the resolution up to the point where variations are small and by monitoring the amplitude of higher modes. Moreover, the poloidal coordinate, $\theta_v$, in VMEC minimizes the energy associated with the high spatial modes reducing the number of poloidal modes needed. The number of flux surfaces, toroidal modes and poloidal modes were obtained through a convergence study. A compromise between accuracy and computational cost is found using 200 radial surfaces and 23 poloidal modes and a different number of toroidal modes depending on the case. The specific harmonics or modes used are, $n = [0]$ for the axisymmetric case $\mathbf{B}_{\mathrm{AXI}}$, $n = [-72, -54, -32, -18, 0, +18, +32, +54, +72]$ for the ripple cases $\mathbf{B}_{\mathrm{ripple}}$ and $n = [-12, -9, -6, -3, 0, +3, +6, +9, +12]$ for $\mathbf{B}_{\mathrm{RMP}}$. As an example, the amplitude of the modes for $\mathbf{B}_{\mathrm{RMP}}$ are shown in Fig. 5 for the last radial surface simulated, i.e. where the displacement is maximum and thus for the most restrictive conditions from the convergence point of view (note the logarithmic scale).

The free boundary equilibria obtained with the VMEC code are shown in Fig. 6 for the axisymmetric (left plot) and RMP fields (center and right plots) cases. Note the complex non-axisymmetric structure for the RMP case. Some parameters of the equilibrium solution are $\hat{a} = 2.6m$ and $\psi_{max} = 120$Wb with a plasma volume of $808\mathrm{m}^3$. The effect of RMP coils on the magnetic surfaces near the plasma edge, generating perturbations in the magnetic surfaces geometry and breaking the axisymmetry can be clearly seen. These results are in good agreement with those obtained by integrated modelling with ASTRA and the SPIDER Grad-Safranov equation solver [26]. The effect that these local magnetic field magnitude variations will have on the particle transport is the topic of next sections.

## 4. SFINCS code benchmarks for axisymmetric and non-axisymmetric equilibria

In this section the neoclassical code SFINCS [21, 22] will be used to calculate the radial transport of particles for the axisymmetric and non-axisymmetric MHD equilibrium previously described. As a first step SFINCS has been benchmarked against the well stablished 2D neoclassical codes NEO [32] and NCLASS [33] both in the core plasma and in the pedestal region, respectively. These benchmarks have been essential to understand

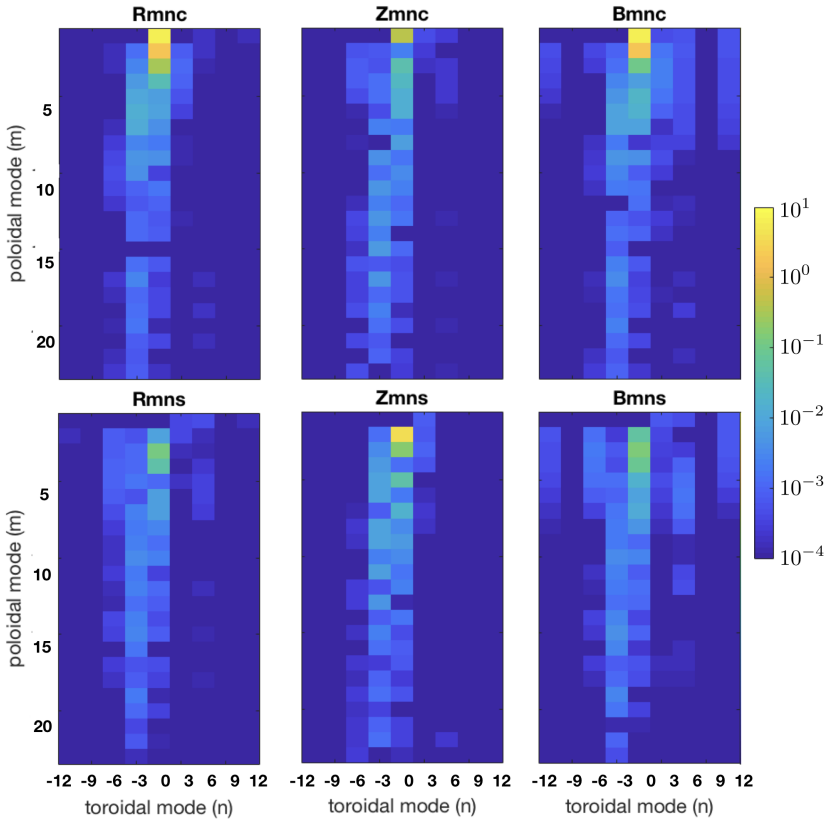


**Figure 5.** Magnitude of the VMEC spectral cosine (top) and sine (bottom) components at the outermost radial surface for the case $\mathbf{B}_{\mathrm{RMP}}$ and, from left to right, the $R$ and $Z$ coordinates and $B$ the field magnitude.

the limitations of the various codes for the calculation of impurity fluxes when the electric field is non negligible. In a second step, SFINCS results have been compared with those of the usual technique used to estimate neoclassical transport in stellarators [18] with the MOCA code [34, 35] for both axisymmetric and non-axisymmetric equilibria.

### *4.1. SFINCS code*

SFINCS is a relatively recent and very successful neoclassical code [21, 22] that solves the stationary state Drift Kinetic Equation (DKE) for the distribution function of the different plasma species for 3D magnetic fields. SFINCS can implement several dynamical models. The one used here will be the so-called *full-trajectories dynamics* which solves the following kinetic equation:

$$\dot{\mathbf{r}}\left(\nabla f_{a1}\right)_{x_a,\xi} + \dot{x}_a\left(\frac{\partial f_{a1}}{\partial x_a}\right)_{\mathbf{r},\xi} + \dot{\xi}_a\left(\frac{\partial f_{a1}}{\partial \xi}\right)_{\mathbf{r},x_a} - \sum_b C^L_{ab} =$$

$$= -\mathbf{v}_{ma}\cdot\left(\nabla f_{a0}\right)_{W_{a0}} + \frac{Z_a e}{T_a} v_{\parallel}\frac{B\left\langle E_{\parallel}B\right\rangle}{\left\langle B^2\right\rangle} f_{a0} + S_a \tag{3}$$

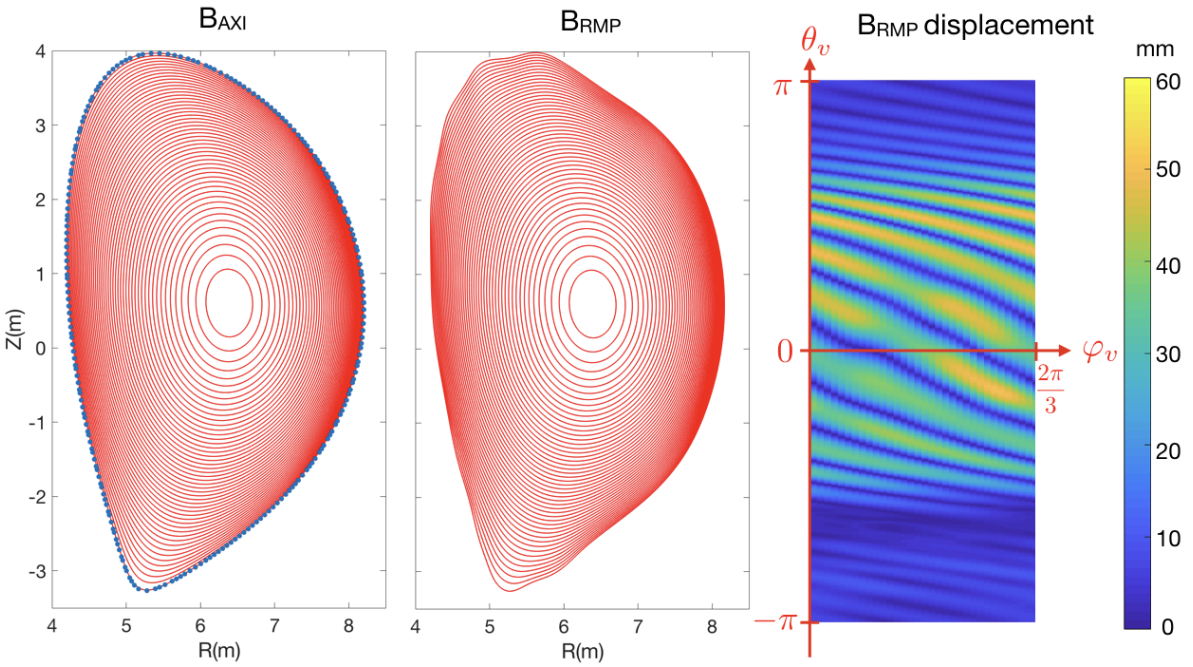


**Figure 6.** Magnetic surfaces, equally spaced in toroidal flux, for the axisymmetric $\mathbf{B}_{AXI}$ (left) and $\mathbf{B}_{RMP}$ equilibria for $\varphi = 0$ (middle). Blue dots shows the LCFS obtained with the ASTRA-SPIDER 2-D solver. Right: Local distance between the unperturbed last magnetic surface for the $\mathbf{B}_{\mathrm{AXI}}$ and $\mathbf{B}_{RMP}$ equilibria for $\phi_U = 45^o$, $\phi_L = 75^o$ as a function of the VMEC toroidal $\theta_v$ and poloidal $\varphi_v$ angles for one period $\varphi_v \in [0, 2\pi/3)$.

with

$$\dot{\mathbf{r}} = v_{\|}\mathbf{b} + \frac{c\mathbf{B}\times\nabla\Phi_0}{B^2}, \tag{4}$$

$$\dot{x}_a = -\mathbf{v}_{ma}\cdot\frac{Z_a e}{2T_a x_a}\nabla\Phi_0, \tag{5}$$

$$\dot{\xi}_a = -\frac{1-\xi^2}{2B\xi}v_{\|}\mathbf{b}\cdot\nabla B + \xi(1-\xi^2)\frac{c}{2B^3}\mathbf{B}\times\nabla\Phi_0\cdot\nabla B \tag{6}$$

where $\mathbf{v}_{ma}$ is the magnetic drift, $\Phi_0$ is the zero order electrostatic potential, $W_{a0} = v^2/2 + Z_a e\Phi_0/m_a$ is the total energy and $f_{a0}$ the zero order Maxwellian distribution function. For more details about the model, refer to [22]. Equation 3 is solved on the $(x_a, \xi)$ space, where $x_a = v/v_a$ and $\xi = v_{\|}/v$. The code can use different collision operators, $C^L_{ab}$ between species $a$ and $b$, from a simple pitch angle scattering to a fully linearized and conservative one, which is essential in axisymmetric geometries to keep intrinsic radial ambipolarity [36]. Under the *small gyroradius ordering*, all first order terms in the expansion are included on the equation. The $E\times B$ drift term, which is of second order, is also included to recover the $1/\nu$ regime in the *long mean free path*, and requires artificial source terms $S_a$ on the SFINCS implementation in order to obtain a stationary solution. However, as shown in [22], these artificial source

terms are usually small and are exactly zero for radial electric fields solution of the ambipolarity condition, i.e. for the cases of interest of this work. Other second order terms are kept on the evolution to keep energy conservation. The poloidal asymmetry of heavy impurity density and electric potential, which has being recently identified as a relevant neoclassical ingredient for general impurities [37, 38] and particularly for tungsten [39] is naturally included in SFINCS through the variations of the first order distribution function of each species and, optionally, the electric potential perturbations $\Phi_1$ on the flux surface. Discarding any other second or higher order terms allows to radially decouple the dynamics, thus allowing the radial position to be considered as a parameter rather than a variable. This *local ansatz* makes the particle distribution of the different species a function of the energy, the toroidal, poloidal and pitch angles, and makes the computational problem more tractable. The small gyroradius ordering along with the local ansatz requires, among other things, the poloidal Larmor radius to be much smaller than the characteristic plasma spatial scales and is on the limit of applicability for the pedestal region where, for the cases under study, $\rho_D \sim 1$ cm and $\rho_W \sim 0.5$ cm, and the density and temperature spatial scales are $L_n \sim L_T \sim 5$ - 10 cm. In principle, global codes such as PERFECT [40] could give more accurate results, but these codes have just been tested for axisymmetric geometries and are still under development for 3D geometries. Throughout this work the radially local version of SFINCS will be used as an initial approximation to the problem. The local particle fluxes for the different species are calculated from flux surface averages of phase space moments of the distribution functions, the local temperature and densities, along with their radial gradients. For general magnetic equilibria (e.g. non-axisymmetric configurations), the intrinsic radial ambipolarity condition is not automatically fulfilled. In these cases, it is necessary to make a scan on the radial electric field with SFINCS to find the value for which radial charge particle fluxes are balanced. This means that a systematic study of transport on these magnetic equilibrium configurations and plasma profiles requires to run SFINCS many times with different radial electric fields. In general, the numerical requirements of SFINCS increase with the complexity of the magnetic equilibrium and decreasing collisionalities. This is related to the steepness of the layer in phase space between the passing and trapped particles. Thankfully, inside the pedestal region, the collisionalities of all the species of interest is sufficiently large to make the computations feasible. Needless to say that systematic scans were made on all code internal discretization parameters until no significant variations in the results were found.

### *4.2. Axisymmetric geometry. Comparison with NEO and NCLASS codes*

Before applying SFINCS to study the effect of breaking axisymmetry due to toroidal field ripple and RMP fields on transport in the pedestal region, SFINCS is compared with two well-established axisymmetric neoclassical codes NEO [32] and NCLASS [33] in plasma conditions where they results should coincide.

NEO is a continuous code that also solves the stationary drift kinetic equation in a way similar to SFINCS by finding the first order distribution function $f_{1a}$ from:

$$v_{\|}\mathbf{b}\cdot\nabla g_{1a} - \sum_b C^L_{ab} = -\mathbf{v}_{ma}\cdot\nabla f_{0a} - \frac{Z_a e}{T_a}\mathbf{v}_D\cdot\nabla\Phi_0 \tag{7}$$

where the parallel electric field has been ignored in the benchmark, since this is very low in ITER high Q plasmas because of the high plasma electron temperature (loop voltage  50 mV). The distribution function $g_{1a} = f_{1a} + f_{0a}(z_a e\Phi_1/T_{0a})$, where $\Phi_1$ is the perturbed part of the electrostatic potential on the flux surface, is a function of the kinetic energy $\varepsilon$ and magnetic moment $\mu$. For more details refer to [32]. The first clear difference when comparing the 2D version of NEO with that of SFINCS (Eq. 3) is the absence of any second order terms (some of which are included in the 3D version of NEO [41]). Though this is justified for axisymmetric devices in the *long mean free path* $1/\nu$ regime, our benchmark has revealed that it is not the case in the collisional Pfirsch-Schlüter regime where transport depends on the $E\times B$ drift. Another difference between SFINCS Eq. 3 and NEO Eq.7 is that NEO dynamics contains a $\Phi_1$ effect, of order $e\Phi_1/T \sim \rho^*$ (see for example [38]). This effect can also be optionally included in SFINCS but, as it will be shown, it is not significant for the ITER conditions considered. The 2D version of NEO has been extensively applied to study neoclassical transport in ITER plasmas and is the first code that we have used in our benchmark [42]. The second code NCLASS is also a standard in the community [33] and is routinely used to model ITER plasmas [26] and calculates the neoclassical transport of multi-species axisymmetric plasmas. In our benchmark we have compared the radial flux, $\Gamma_a$, and the values of the diffusion coefficient $D_a$ and pinch velocity $V_a$ for the different species ($a$). $D_a$ and $V_a$ are indirectly obtained by modeling the radial particle flux as

$$\Gamma_a = -D_a\frac{dn_a}{dr} + n_a V_a, \tag{8}$$

where $V_a$ contains the interactions with other species, including the temperature screening. Since SFINCS, NEO and NCLASS are linear codes, the values of $V_a$ and $D_a$ are obtained by running two simulations for each species. In a first simulation, the density gradient is set to zero to obtain $V_a$ from the particle flux as

$$V_a = \frac{\Gamma_a|_{\frac{dn_a}{dr}=0}}{n_a}. \tag{9}$$

In a second simulation the diffusion coefficient $D_a$ is obtained restoring the density gradient

$$D_a = \frac{n_a V_a - \Gamma_a}{\frac{dn_a}{dr}}. \tag{10}$$

This process has to be repeated for each species. The particle fluxes for D, T and W corresponding to the ITER reference scenario of Section 2 and the equilibrium $\mathbf{B}_{\mathrm{AXI}}$ from Section 3 is presented in the two upper plots of Fig. 7 for the case of $E_r = 0$. SFINCS results are compared in the core plasma (left) with those of NCLASS and in the pedestal region (right) with NEO. For this comparison NEO calculations include the

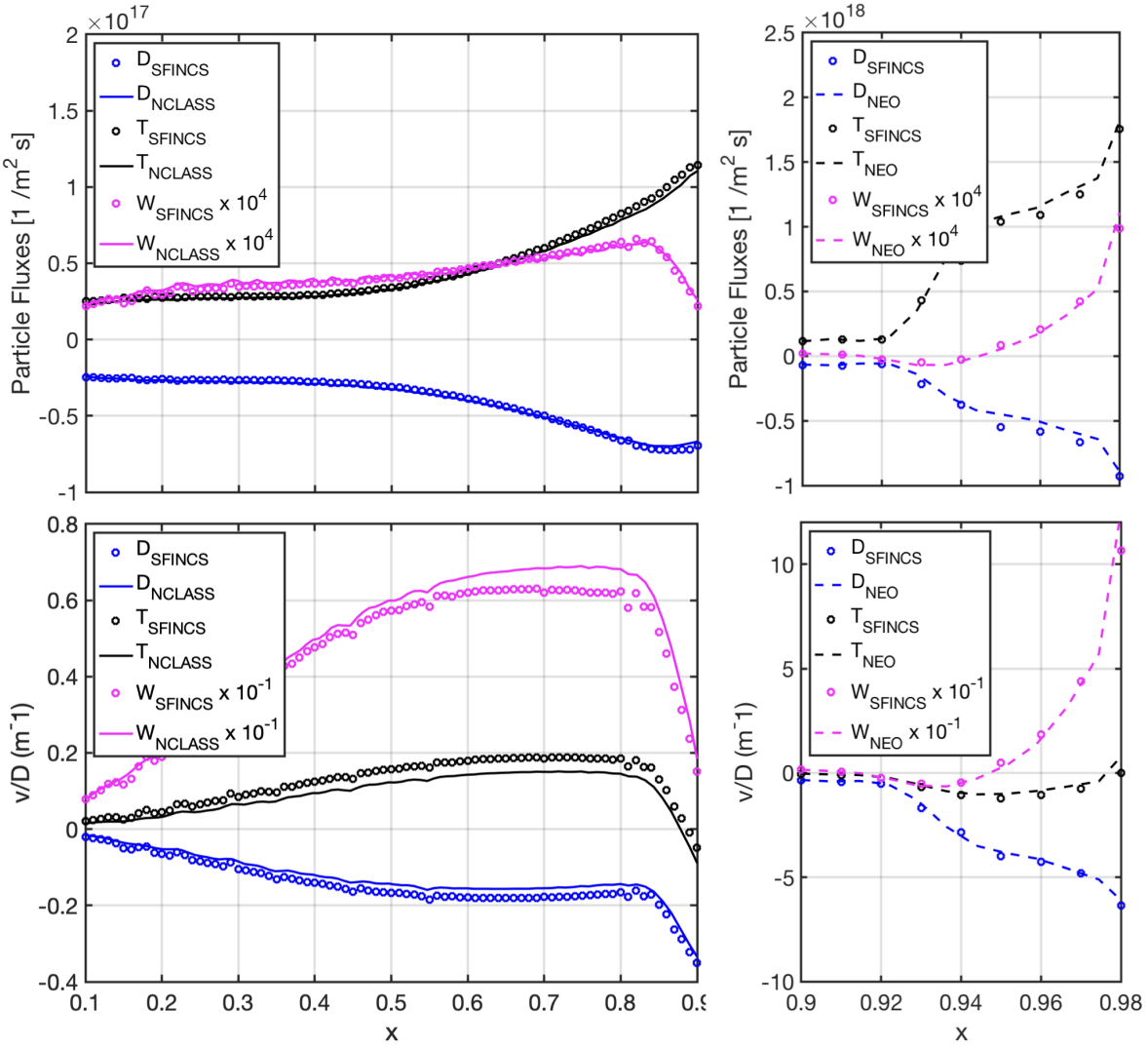


**Figure 7.** Particle fluxes (top) and $V/D$ (bottom) on the inner region of the plasma (left) and in the pedestal (right) for the ITER reference scenario of Section 2 and the equilibrium $\mathbf{B}_{\mathrm{AXI}}$ from Section 3. The quantities has been calculated with NCLASS, NEO and SFINCS codes. Note that the results for tungsten have been scaled by different factors in each plot to fit in the plot.

potential variation on flux surfaces, $\Phi_1$, while SFINCS does not. Despite this, excellent agreement is found in all cases for all species. We have also checked that including the effects of $\Phi_1$ on SFINCS calculations (this requires an extra non-linear iteration loop in the algorithm) does not change the results. For the conditions under study, the benchmark indicates that the effect of $\Phi_1$ is small, at least up to $Z = 20$ and $E_r = 0$. As shown in the figure the deuterium particle flux has different sign from to tritium as already identified in [42] due to its lighter mass. Also to be noted is the large increase of all fluxes in the pedestal region with a change in the sign of tungsten flux due to the strong temperature screening in the ITER pedestal [2]. In the two lower plots of Fig. 7 the ratio of pinch velocity to diffusion coefficient $V/D$ is shown for the same conditions,

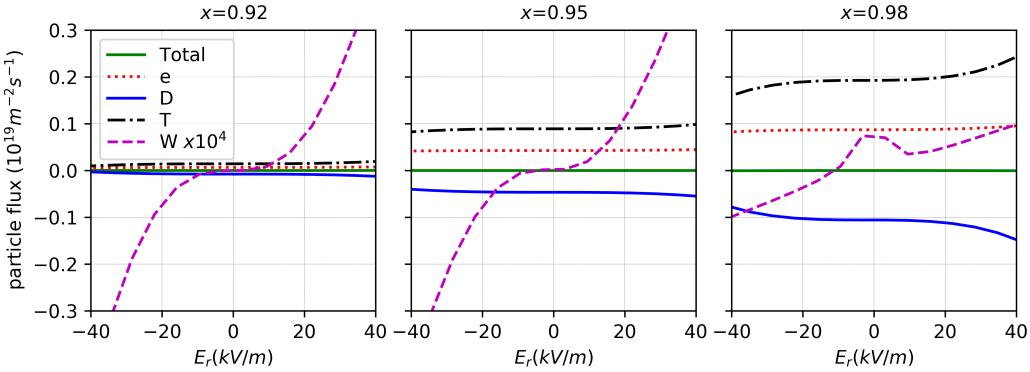


**Figure 8.** Particle fluxes of the different species versus the radial electric field $E_r$ calculated with SFINCS for three positions inside the pedestal region, x=0.92, 0.95 and 0.98 (from left to right) for the axisymmetric case. The green curve represents the radial current $J_r/e$.

where again, there is a good agreement between the codes. Extensive studies on tungsten transport have compared the predictions of neoclassical and anomalous transport codes with experimental measurements (e.g. references 1-10 in [2]).

The results shown in Fig. 7 have been evaluated for $E_r = 0$. In the neoclassical ordering, the flux of the different species is expected to be independent on the electric field to first order. Indeed, it has been checked that the fluxes calculated with NEO, which only includes first order terms, does not depend on $E_r$ for any of the species, including tungsten. On the other hand, particle fluxes calculated with SFINCS are almost insensitive to $E_r$ up to $20 - 30kV/m$ for the main species but show a rather strong dependence for tungsten, see Fig. 8. To understand the discrepancy between both codes for finite $E_r$ it has to be recalled that, when the poloidal ion Mach number $M_p = (B/B_{pol})|\mathbf{v}_E|/v_i$ reaches order O(1), the first order approximation is not accurate anymore and the radial electric field is expected to modify the neoclassical fluxes [22, 43]. In fact, for the benchmark conditions of ITER pedestal plasmas, the value of the Mach poloidal number for $E_r = 20kV/m$ is $M_p^e \sim 5 \times 10^{-4}$ for the electrons, $M_p^D, M_p^T \sim 0.04$ for the main species and $M_p^W \sim 0.4$ for tungsten, which breaks the small poloidal Mach number approximation for tungsten and is due to its large mass. This approximation applies for $E_r \approx 0$ because the poloidal Mach numbers in this case are zero. The discrepancy between NEO and SFINCS results for finite $E_r$ is then related with the $E \times B$ drift term included in the SFINCS dynamics, see Eq. 3, but not on the 2D version of NEO, see Eq. 7. Not only the effect of the mass, but also the large value of the tungsten charge increases the effect of the RHS of Eq. 3 associated with the electrostatic potential, reducing the minimum value of $E_r$ where its effect is noticeable. The choice of $Z_W = 20$ for our studies thus ensures that the effects identified will be applicable to all tungsten ionization states existing at the ITER plasma pedestal since this is a lower limit for the tungsten charge in the plasma conditions studied. In fact, if

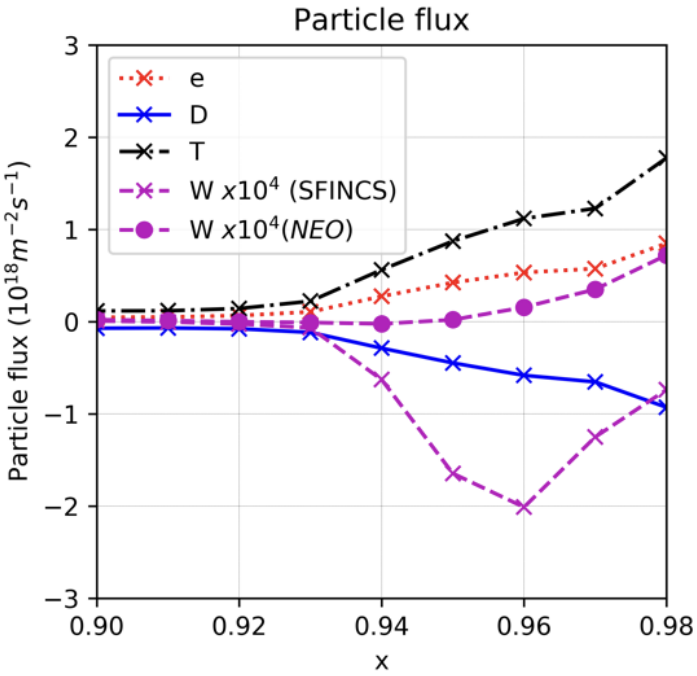


**Figure 9.** Particle fluxes of the different species across the pedestal for the radial electric field profile derived from force balance considerations for axisymmetric equilibria. The tungsten flux is shown as evaluated both with NEO and SFINCS.

the $E \times B$ drift term is eliminated from SFINCS dynamics, particle fluxes are found to be completely independent to $E_r$, even for tungsten, thus replicating NEO results. It, however, remains to be determined if the tungsten fluxes are accurately calculated by SFINCS for the ITER plasma conditions studied since they do not include all second order terms in the dynamics. Obtaining the accurate fluxes for high $M_p$ is an open issue [41] except for axisymmetric configurations for some particular conditions [43, 44]. To our knowledge, there is still no simple model or code that can reliably obtain the neoclassical transport for large poloidal mach number impurity flows in 2D and 3D non-axisymmetric geometries. The agreement between 2D and 3D codes in our benchmark shows that main species particle transport can be accurately described for electric fields up to $E_r \sim 20 - 30kV/m$ in ITER pedestal plasmas, but only for $E_r \sim 0$ in the case of tungsten. However, this does not mean that some conclusions cannot be drawn even for the case of tungsten radial transport. Finally, note that the radial current

$$J_r = \sum_{a}^{species} q_a \Gamma_a \tag{11}$$

with $\Gamma_a$ being the radial fluxes of the different species, is zero for the SFINCS results over the full range of $E_r$ studied (green curve on Fig. 8). This implies that intrinsic ambipolarity is maintained and is a good demonstration of the collision operator conservative properties. NEO also shows excellent results on this respect.

The fluxes of the different species can be calculated inside the pedestal region for a specific choice of the radial electric field, for example the commonly used theoretical approximation [45], valid under the assumption of small toroidal and poloidal main ion flow, given by:

$$E_{theory} \approx \frac{\nabla p_i}{e n_i} \approx \frac{\nabla(n_D T_D + n_T T_T)}{e(n_D + n_T)} \tag{12}$$

The result can be found on Fig. 9, where the tungsten flux is presented for both SFINCS and NEO. Whereas the main ion fluxes (D and T) are very similar for both codes, tungsten flows are different. While for NEO tungsten goes radially outwards in the pedestal, in agreement with previous evaluations [2, 42], for SFINCS the tungsten flow is inwards. Despite the relevance that the tungsten flow direction in the pedestal has on ITER operation and performance it is still not possible to conclude the direction of this flow since no code is able to deal with the high poloidal Mach number of tungsten. Further analysis is required to determine whether the description of the dynamics included in both codes is sufficient/appropriate to evaluate neoclassical tungsten transport accurately enough for the ITER pedestal conditions, including the expected values of the radial electric field. Since the 2D version of NEO, and also NCLASS, cannot be used when the equilibrium configuration is not axisymmetric, the next benchmark step that we have performed is to compare SFINCS with a neoclassical code that can deal with 3D magnetic configurations.

### *4.3. Monoenergetic coefficients. Comparison with MOCA code for axisymmetric and non-axisymmetric equilibria*

For non-axisymmetric systems, the *local ansatz* and the incompressible $E \times B$ approximation [46], which holds for moderate radial electric fields, makes the DKE kinetic energy approximately conserved. This not only reduces the dimensionality of the DKE again, using the energy as a parameter rather than a variable, but also allows simplifying the collision operator and using a simple pitch angle scattering operator. Under these approximations, neoclassical transport can be described by the linearized DKE [47]. Different methods have been used in the stellarator community to obtain the three relevant *monoenergetic* transport coefficients which are the flux surface averaged moments of the solution of this equation. Using the neoclassical formalism [18], the flux-surface-average flows $I_i$:

$$I_1 = \langle \mathbf{\Gamma} \cdot \Delta r \rangle \,, \quad I_2 = \left\langle \frac{\mathbf{Q}}{T} \cdot \nabla r \right\rangle, \quad I_3 = \frac{\langle \mathbf{J} \cdot \mathbf{B} \rangle}{q B_0} \tag{13}$$

can be calculated as:

$$I_i = -n \sum_{j=1}^{3} L_{ij} A_j \tag{14}$$

where the operator $\langle\cdot\rangle$ means flux surface averaging and where the thermodynamic forces $A_j$ are defined as:

$$A_1 = \frac{1}{n}\frac{dn}{dr} - \frac{qE_r}{T} - \frac{3}{2T}\frac{dT}{dr}, \quad A_2 = \frac{1}{T}\frac{dT}{dr}, \quad A_3 = -\frac{qB_0\left\langle \mathbf{E}\cdot\mathbf{B}\right\rangle}{T\left\langle B^2\right\rangle} \tag{15}$$

and the transport coefficients:

$$L_{ij} = \frac{2}{\sqrt{\pi}}\int_0^\infty dK\sqrt{K}e^{-K}D_{ij}(K)h_ih_j \tag{16}$$

with $h_1 = h_3 = 1$, $h_2 = K = (v/v_{th})^2$. The parameters $B_0$, $n$ and $T$ are, respectively, the reference magnetic field, the density and the temperature of the species under study. The integral over $K$ is an energy convolution of the mono-energetic coefficients, $D_{ij}$ related with flux surface averaged moments of the distribution function, with the local Maxwellian. In the absence of parallel electric field, Eq.13, 14 and 15 show that to describe the particle radial transport it suffices to calculate just one coefficient $D_{11} = D_{12}$. To be consistent with the literature, the coefficients and the collisionalities are normalized:

$$D_{11}^\star = D_{12}^\star = \frac{D_{11}}{D_{11}^p}, \quad D_{11}^p = \frac{\pi}{4}\frac{v_d^2R_0}{\iota v} \tag{17}$$

$$\nu^\star = \frac{\nu R_0}{\iota v} \tag{18}$$

being $v$ the velocity of the particle, $v_d = mv^2/(2qR_0B_0)$ the characteristic radial drift velocity, $\iota$ the rotational transform, $R_0$ the reference major radius,$D_{11}^p$ the tokamak *Plateau* value and $\nu$ the deflection collision frequency given by:

$$\nu \equiv \nu^\alpha = \sum_\beta \nu^{\alpha/\beta} \tag{19}$$

this is, the sum of the monoenergetic particle of species $\alpha$ collisions with all the other species $\beta$. Here [48]:

$$\nu^{\alpha/\beta} = \nu_0^{\alpha/\beta}\left[erf\left(\sqrt{K^{\alpha/\beta}}\right)\left(1 - \frac{1}{2K^{\alpha/\beta}}\right) + \sqrt{\pi K^{\alpha/\beta}}\exp(-K^{\alpha/\beta})\right] \tag{20}$$

and:

$$\nu_0^{\alpha/\beta} = \frac{n^\beta\left(q^\alpha q^\beta\right)^2(\ln\Lambda)^{\alpha/\beta}}{4\pi\left(\epsilon_0 m^\alpha\right)^2 v^3} \tag{21}$$

being $K^{\alpha/\beta} = (m^\beta/m^\alpha)(T^\alpha/T^\beta)K$, $\epsilon_0$ the vacuum permittivity and $\ln\Lambda$ the Coulomb logarithm. The advantage of using this mono-energetic technique to estimate neoclassical transport is that it reduces to calculating the integral of Eq 16 for every particle species. Something that can be trivially done if the monoenergetic coefficients, $D_{11}$, are precomputed for a sufficient range of radial positions, collisionalities and radial electric fields. A heavy computational task, especially at very low collisionalities and for complex 3D equilibrium configurations, that thankfully must be done just once.

It is important to understand that SFINCS can operate under different approximations and solves different equations. SFINCS can calculate the monoenergetic coefficients, but can also estimate particle transport using a conservative collision operator where the total energy of the bulk plasma is conserved, but not the energy of each particle individually. As stated above, the monoenergetic treatment is just an approximation. The reason for comparing the monoenergetic coefficients of SFINCS with another code using this method is twofold. The first one is technical, since it allows checking the number of modes required internally in SFINCS to properly describe the collisional regimes relevant for the ITER pedestal region. The second one is practical; the monoenergetic treatment is potentially much faster than SFINCS, if the approximations required are fulfilled. Unfortunately, for the ITER non-axisymmetric equilibria to be studied here, it is not clear where the transition between axisymmetry and broken symmetry occurs, since the 3-D deviations from the 2-D equilibrium are small. Thus it is not clear where intrinsic ambipolarity, requiring momentum conserving methods, is needed and where the monoenergetic treatment can be used.

There are several numerical codes in the stellarator community that can calculate the monoenergetic diffusion coefficients for arbitrary magnetic and radial electric fields, see Ref [18] for a detailed review. Here the $\delta f$ Monte Carlo version of the MOCA [34, 46] code will be used. MOCA solves the first order linearized DKE equation using the method of *characteristics* being the guiding center trajectories of a set of particles the characteristic curves. The integration process is speed-up by pre-storing the magnetic field and its derivatives on a 3D grid. The effect of collisions in the DKE is simulated by applying a pitch angle collision operator [49].

The effect of the equilibrium magnetic field on the monoenergetic diffusion coefficient $D_{11}^*$ is presented in Fig. 10 as a function of collisionality and normalized radial electric field for a position in the pedestal region, $x = 0.97$, for the toroidally symmetric ITER model $\mathbf{B}_{\mathrm{AXI}}$, two $\mathbf{B}_{\mathrm{ripple}}$ equilibria with 1% and 2% toroidal field ripple and a case with the maximum nominal ELM control coil currents leading to the larges RMP field $\mathbf{B}_{RMP}$. The collisionality bounds have been chosen to cover the relevant pedestal range, as will be shown in a later section. More in detail, the results for the axisymmetric equilibrium display the usual tokamak behavior with a Pfirsch-Schlüter regime proportional to $\nu^*$ at high collisionalities, followed by a mild *Plateau* regime and finishing with a *banana* regime also proportional to $\nu^*$ in the long mean free path regime (*lmfp*). As expected, $D_{11}^*$ is independent of the radial electric field except for the suppression of the Pfirsch-Schlüter regime at very large values because of the $\mathbf{E} \times \mathbf{B}$ drift. The effect of breaking axisymmetry is clear for low collisionalities and small radial electric fields with the appearance of a $1/\nu^*$ regime, see the two upper plots of Fig. 10. This regime is suppressed at higher radial electric fields by the $\mathbf{E} \times \mathbf{B}$ rotation, going from an intermediate $\sqrt{\nu^*}$ to a banana $\nu^*$ regime [16] that can be seen in the two lower plots of Fig. 10. The strong reduction of $D_{11}^*$ to the $1/\nu^*$ regime in the high collisionality, Pfirsch-Schlüter regime is due to the $E \times B$ second order drift term retained in SFINCS dynamics. In fact, the reduction of the tungsten flux for moderate

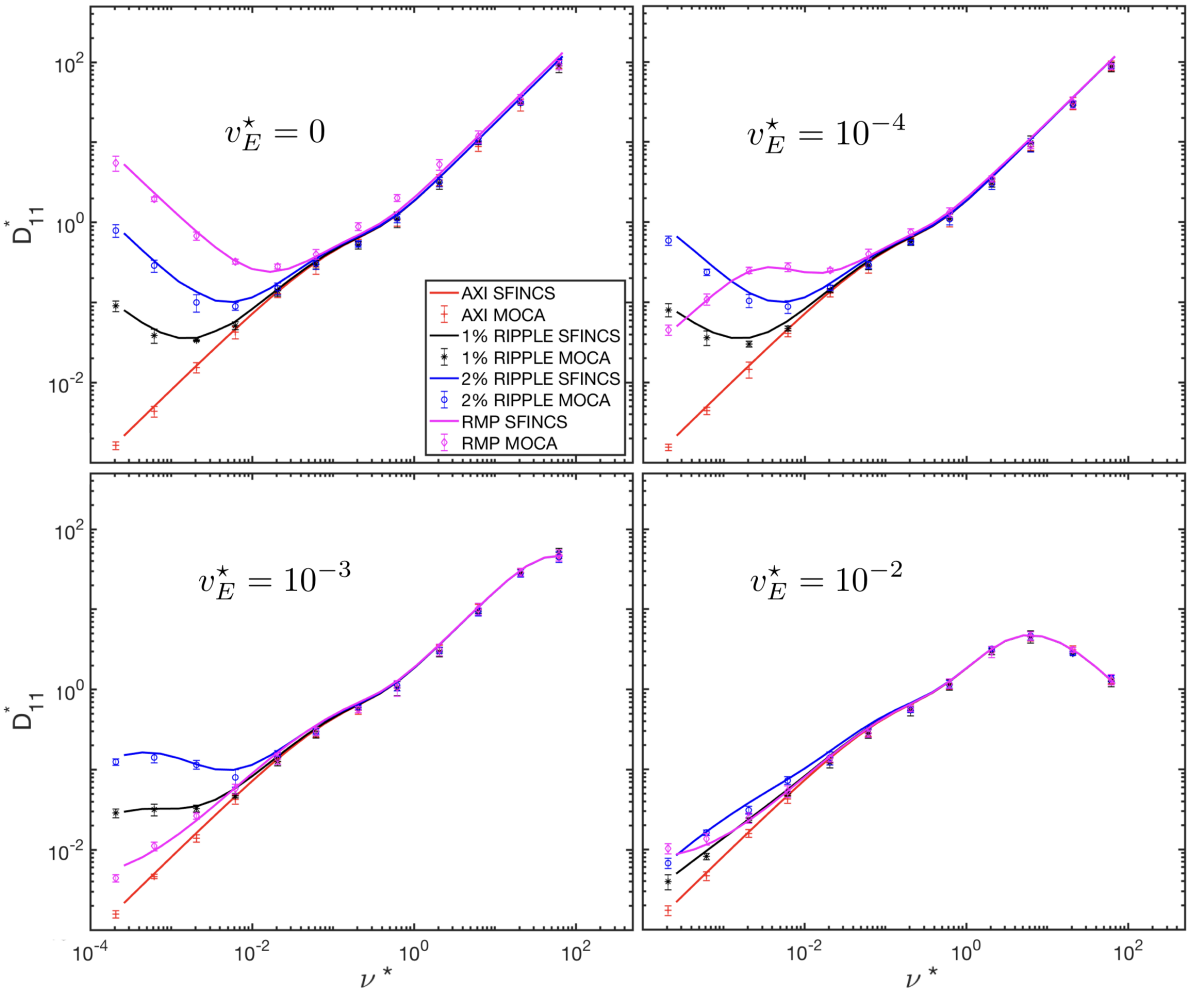


**Figure 10.** Monoenergetic coefficient $D_{11}$ as a function of the collisionality $\nu^\star$ for the radial position $x = 0.97$ calculated with SFINCS and MOCA for the equilibria described in Section 3 for the normalized radial electric fields $v_E^\star = E_r/(vB_0) = 0$ (top left), $10^{-4}$ (top right), $10^{-3}$ (bottom left) and $10^{-2}$ (bottom right).

electric fields at the pedestal edge $x = 0.98$, where the collisionality is highest, in Fig. 8 is an indication of Pfirsch-Schlüter suppression.

The general agreement between SFINCS and MOCA, both using a pitch angle collision operator, in all conditions is fairly good when one considers the very different numerical discretization used (particles versus continuous). In the case of MOCA, for each energy calculation, 1024 particles are run for several collisional times. As for SFINCS, the simulations were used to adjust the number of modes needed in the discretization of the poloidal ($N_{theta} = 80$), toroidal ($N_{zeta} = 15$) and pitch angles ($N_{xi} = 100$) for each energy.

If a conservative collision operator were applied on MOCA test-particles (equivalent to collisions with a non-static background), the effect of the electric field on Eq. 15 would be compensated for axisymmetric geometries, recovering the insensitivity of the

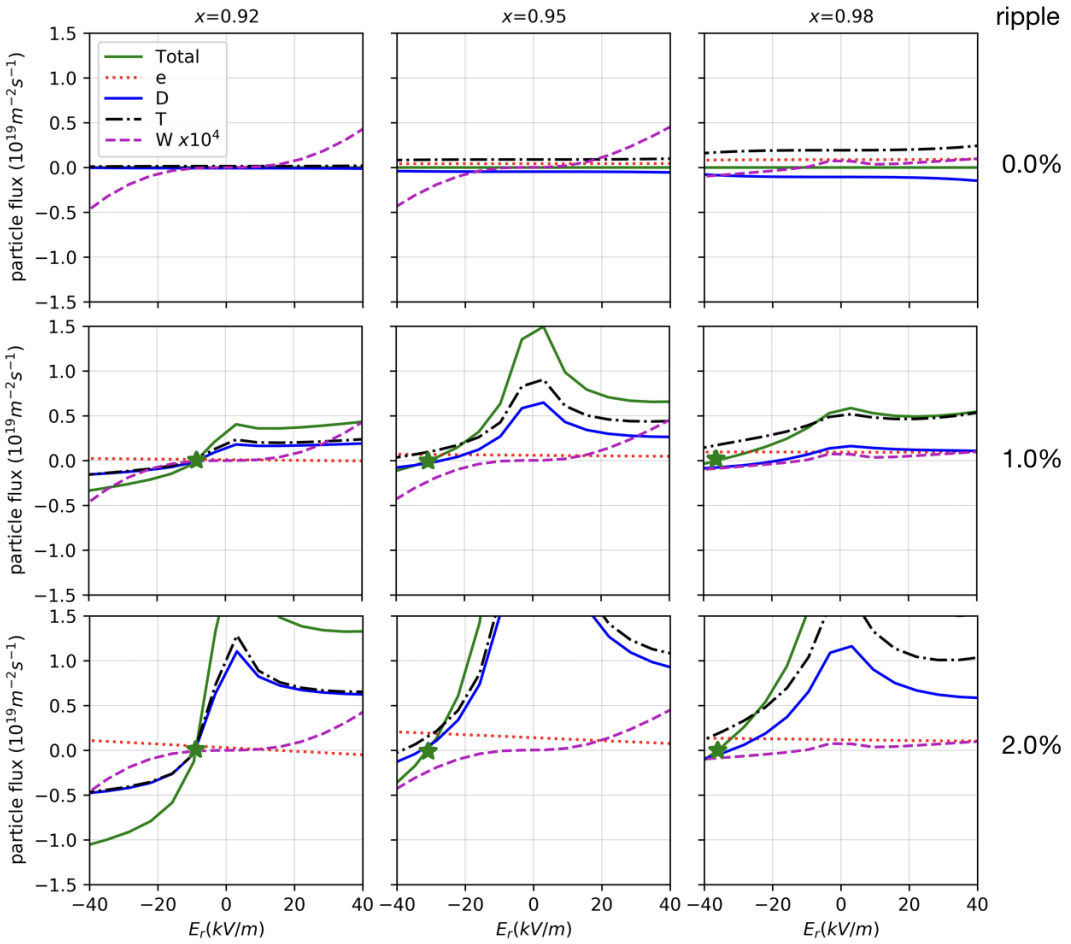


**Figure 11.** Particle flux of the different species versus the radial electric field $E_r$ for three positions inside the pedestal region, x=0.92, 0.95 and 0.98 (from left to right) and three toroidal field ripple values 0%, 1% and 2% (from top to bottom). The green curve represents the radial current $J_r/e$.

radial flux to $E_r$ on such geometries for small Mach numbers. However, the difficulty of introducing the field part of the full collision operator in Monte Carlo codes, has led to the use of SFINCS instead of MOCA for the calculations of the electron, deuterium, tritium and tungsten fluxes in our studies described in Sec. 5 for equilibria with toroidal field ripple and in Sec. 6 for equilibria with RMP fields.

## 5. Non axisymmetric perturbations: effect of the toroidal field ripple

The effects of the toroidal field ripple on the neoclassical particle fluxes has been studied in a range of ripple amplitude from 0.0% to 2.0%, using the magnetic equilibria $\mathbf{B}_{\text{ripple}}$ described on Sec 3. Fluxes of the different species calculated with SFINCS are represented as a function of the radial electric field in Fig. 11 for different radial positions inside the pedestal (from left to right) and ripple amplitudes (from top to bottom). These results were obtained solving with SFINCS the four dimensional

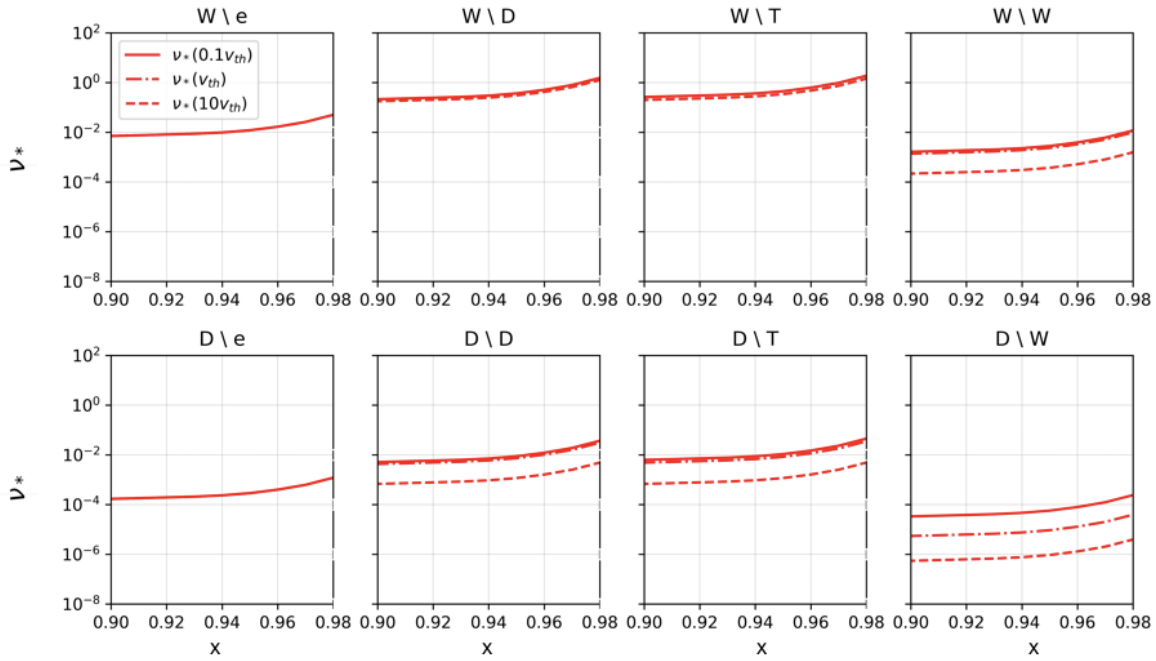


**Figure 12.** Collisionality $\nu^*$ profiles for test particles in the pedestal region, labelled with the NRL Plasma Formulary [48] convention $\alpha\backslash\beta$. The collisionalities are calculated for three monoenergetic test energies corresponding to 0.1, 1 and 10 times the thermal velocity for $\alpha$ species: tungsten (upper row) and deuterium (lower row). From left to right, collisions are considered with a $\beta$ background of electrons, deuterium, tritium and tungsten ions.

q.

(toroidal, poloidal, pitch and energy) DKE equation of each of the four populations (electron, deuterium, tritium and tungsten) coupled by the linearized conservative collision operator between them, for every radial position. It can be seen that the effect of the ripple on the fluxes of the main species is strong but, as it will be shown later, under ambipolar electric field it only starts to be noticeable around 1.0% and above. It is important to mention here that ITER toroidal field ripple for $Q = 10$ plasmas at 5.3T is expected to be around 0.3%, thanks to the ferromagnetic inserts. However, higher levels of ripple will occur for lower toroidal field plasmas to be explored earlier in the Pre-Fusion Operation phase of the ITER Research Plan (≈0.55% at 2.65T ≈1.3% for 1.8 T) [4]. Our studies indicate that ripple effects may be significant for 1.8T plasmas but not at 2.65T but this need to be confirmed with dedicated simulations since the collisionality of these lower toroidal field H-mode plasmas is different from that of $Q = 10$ plasmas and this is an important factor in determining the effects of toroidal field ripple on neoclassical transport. Another interesting effect seen in Fig. 11 is the strong dependence of electron, deuterium and tritium particle fluxes for ripple values above 1.0% compared to the independence of tungsten fluxes on the ripple level (note that open issues remain for tungsten particle fluxes with high values of the electric field in

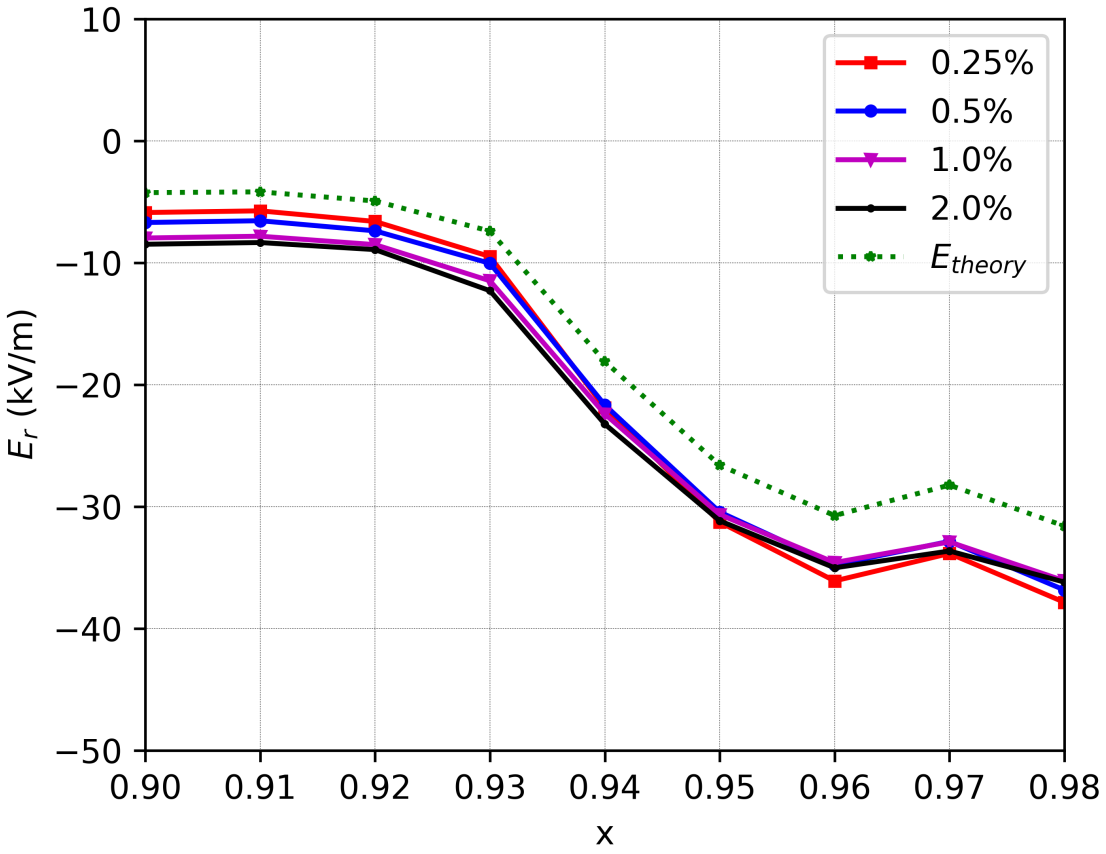


**Figure 13.** Ambipolar radial electric field profile in the pedestal region as a function of the value of the toroidal field ripple.

the ITER pedestal due to second order neoclassical effects, as discussed in Sect. 4). To understand this result it is helpful to remember the monoenergetic picture of Section 4.3 for the relevant collisionalities of the different species. To this end, in Fig. 12 the radial dependence of tungsten (top) and deuterium (bottom) collisionalities with the rest of the species are shown for three energies. In the pedestal, the dominant process for tungsten is the collision with deuterium and tritium giving a $\nu^*$ between $10^{-1}$ and 1, independently on the tungsten energy. The results of Fig. 10 for this collisional range, corresponding to the *Plateau regime*, show that monoenergetic diffusion coefficients are independent of the electric field. We note here that this effect would be even stronger for larger values of $Z_W > 20$ because of the dependence of collisionality with charge, see Eq. 21. This is the reason why have chosen a relatively low value $Z_W = 20$ compared to that expected in the ITER pedestal ($Z_W = 20$ is adequate near the separatrix but too low for the pedestal top); in this way we ensure that effects identified in the neoclassical transport for this charge level are valid for all tungsten ionization states in the pedestal. On the other hand, the collisional range for the main ion species of the plasma (see for example

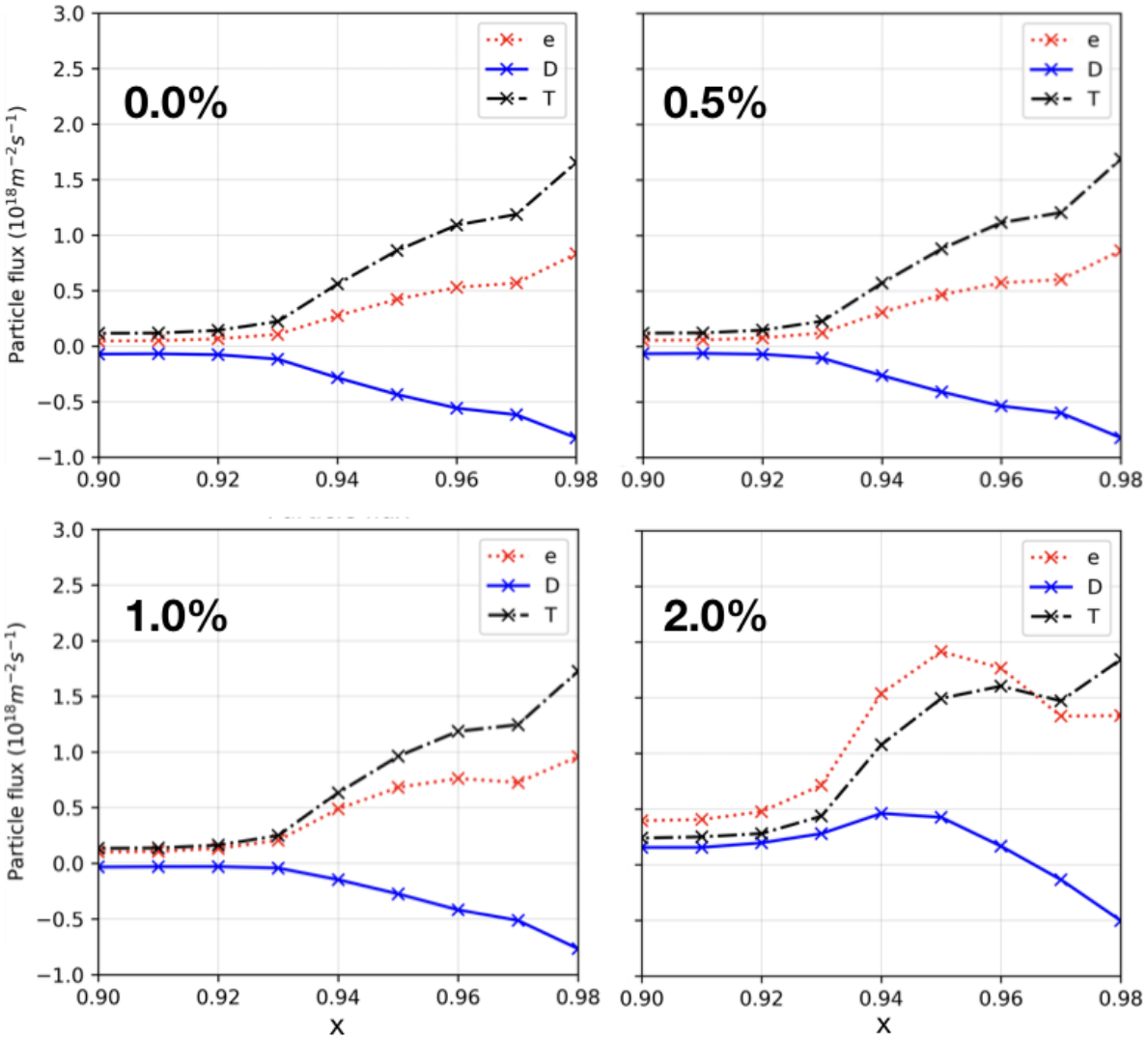


**Figure 14.** Ambipolar particle flux profiles in the pedestal region for all species as a function of the ripple for 0.0% (top left), 0.5% (top right), 1.0% (bottom left), 2.0% (bottom right).

the deuterium in Fig. 12) $\nu^* \sim 10^{-3} - 10^{-2}$ corresponds to the $\sqrt{\nu}^*$ or $1/\nu^*$ regimes (see Fig. 10) which are sensitive to the non-axisymmetric perturbation of the magnetic equilibria that modify particle trajectories. The range of collisionalities studied here allows reducing the resolution ($N_{theta} = 80$, $N_{zeta} = 7$ and $N_{xi} = 80$ and $N_x = 8$) with respect to Section 4.3 such that SFINCS can run in reasonable computational times. Note that to solve the four dimensional (non-monoenergetic) DKE a discretization in energy through $N_x$ is required.

Since no external charge is injected in the ITER plasmas, the radial current $J_r$ should be zero, a condition implying that in stationary state the plasma should not accumulate charge. In axisymmetric equilibria this condition is automatically satisfied for any value of the radial electric field, result of momentum conservation. The value of

the total radial current as a function of the electric field for the different ripple values is shown in Fig. 11 with a green line (radial current divided by electron charge $J_r/e$). In the axisymmetric case, perfect ambipolarity for all electric fields is found, which is an excellent demonstration of SFINCS conservation capabilities. However, when non-axisymmetric ripple perturbations are included, the ambipolarity condition is only fulfilled for certain values of the radial electric field, called roots. These are solutions of the ambipolar condition, i.e. for which the electron radial current is equal to the sum of the radial currents of all ion species. The values of the roots, marked on the plots with a star for the ripple cases, are found as the crossing through zero of the total radial current‡. The roots will be stable if the derivative of the flux with respect to the electric field is positive (i.e. if the plasma is positively charged, the tendency of the particle flux is to expel the positive charges, finding a stable equilibrium). For all the ripple cases only one stable root is found in the electric field range studied. The ambipolar radial electric field profile in the pedestal is shown in Fig. 13 for four values of the ripple, 0.25%, 0.5%, 1% and 2% along with the 2-D force-balance electric field (see Eq. 12). These results clearly show that the impact of toroidal field ripple on the ambipolar field is very small, even at for ripple values of a 2.0% which exceed by almost an order of magnitude those expected in ITER $Q = 10$ operation. An assessment for Pre-Fusion Operation plasmas in ITER, which have a higher value of the toroidal ripple will be performed to determine if the results obtained for 15 MA/5.3 T Q = 10 plasmas apply to these earlier H-mode scenarios. The small discrepancy found between the theoretical approximation and SFINCS calculation might be due to the fact that Eq. 12 assumes that the electron flux is much smaller than the ion flux, which is not always the case for our conditions, and ignores the poloidal rotation in the force balance electric field evaluation.

The particle flux profiles in the pedestal region for all the species corresponding to the ambipolar values of the radial electric field is shown in Fig. 14 as a function of the ripple level. For the axisymmetric case, the theoretical electric field was used because of the intrinsic ambipolarity of these equilibria. Significant variations in the main species fluxes can only be found for the unrealistically high ripple value for ITER of 2% for $Q = 10$ plasmas, at which the deuterium flux even reverses direction. As previously mentioned, SFINCS also offers the possibility to introduce the effect of the potential perturbation inside of the surface $\Phi_1$. However, it has been checked that its effect is not quantitatively significant for the conditions studied and thus does not affect the conclusion presented here. A detailed study including variations of plasma potential on the 3-D equilibria flux surfaces will be carried out in the future.

Therefore we can conclude that, for the ripple levels and the plasma conditions expected in ITER $Q = 10$ plasmas, neither the pedestal transport of the main species nor the ambipolar electric field are expected to change with respect to the axisymmetric situation. Pedestal tungsten collisionality is high enough such that no direct effect of the

‡ The tungsten flux is neglected when calculating the radial current, an approximation fully justified because of the low tungsten concentration ($10^{-6}$ compared to the main species).

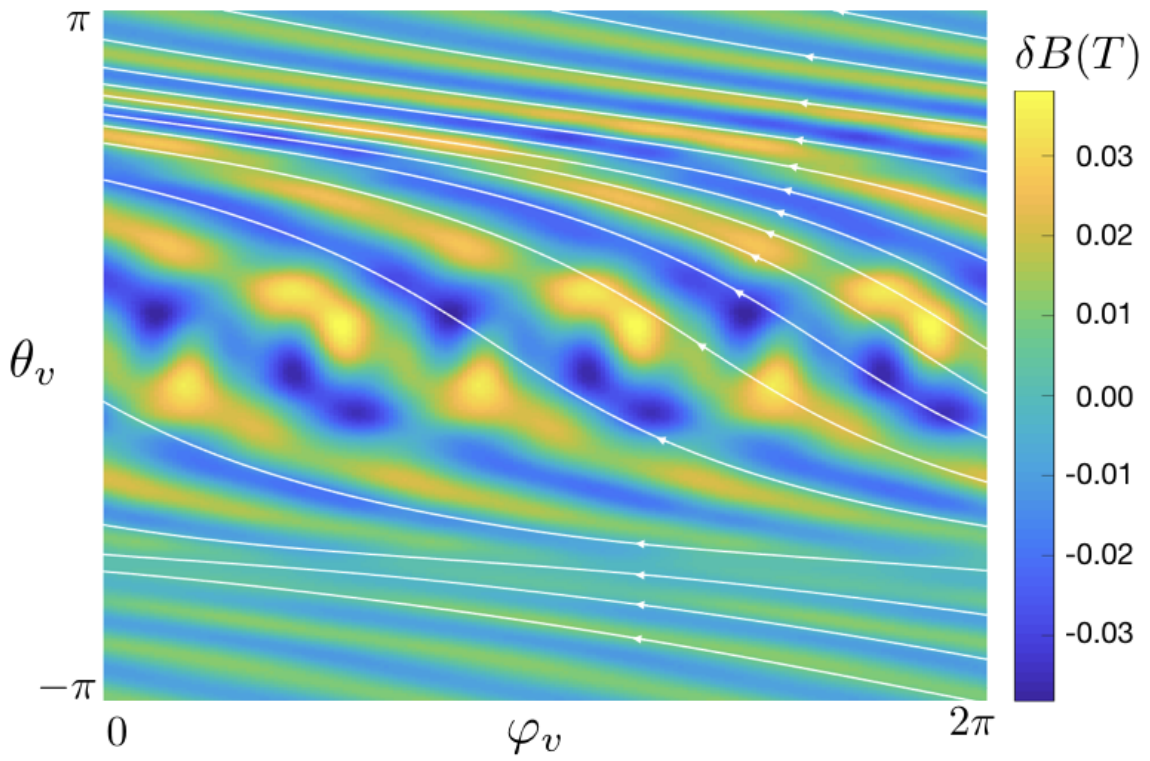


**Figure 15.** Variation of the magnetic field $\delta B = B - \langle B \rangle_\varphi$ on the LCFS for the $\mathbf{B}_{RMP}$ MHD equilibrium as a function of the VMEC toroidal $\varphi_v$ and poloidal $\theta_v$ coordinates. The magnetic field lines are shown in white. Note the $n = 3$ periodicity of the perturbation.

ripple on the impurity neoclassical fluxes is found either. An assessment of these effects for H-mode plasmas to be explored in advance of $Q = 10$ operation with lower toroidal field and larger ripple values (0.55 - 1.3%) will be performed to determine if this result applies to all ITER H-modes or only to those at 5.3T. Thus, previous results obtained in [2] should be relevant also even in the presence of ripple with the important caveat discussed above of the applicability of the first order neoclassical transport modeling for high values of the pedestal electric field and the high poloidal Mach numbers of tungsten in this region. But this is not dependent on the ripple value, as shown on Fig. 13. In the next section, we study the application of RMP fields, where some interesting differences with respect to the toroidal field ripple are found.

## 6. Non axisymmetric perturbations: RMP fields

The last case studied is the effect of the non-axisymmetric fields created by the ELM control coils on particle transport. The procedure followed is analogous to that of the ripple studies, except for the resolution required in the SFINCS simulations that is higher in the spatial coordinates, especially in the poloidal direction. This is needed because of the more complex magnetic field structure created with the RMP fields (see Fig. 15).

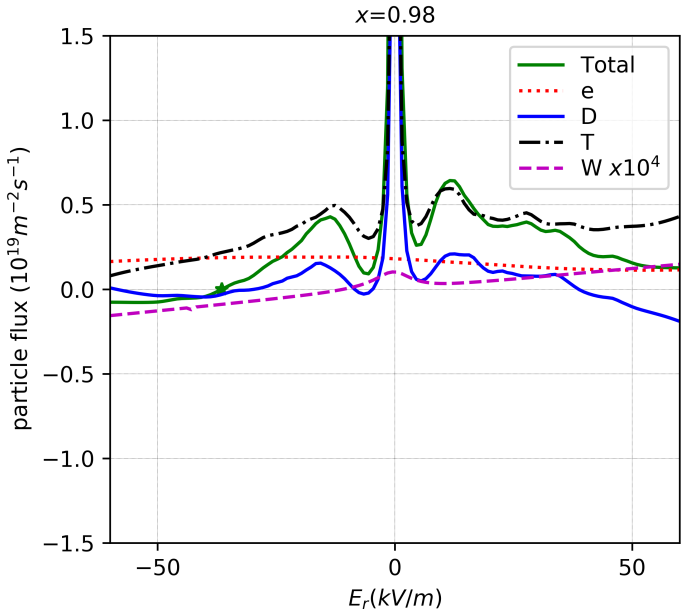


**Figure 16.** Particle fluxes at radial position $x = 0.98$ with the ELM control coils carrying the maximum current of 90 kAturn thus creating the largest RMP fields.

The fluxes of all the species are shown in Fig. 16 at the radial position $x = 0.98$, where we have used the following resolution $N_{theta} = 161$, $N_{zeta} = 12$, $N_{xi} = 40$ and $N_x = 8$ for each of the three toroidal periods considered. The tungsten flux is found to be virtually identical to that of the axisymmetric case (see Fig. 11) even in these conditions, for which the largest RMP fields possible in ITER have been considered. This is due to the very weak dependence of neoclassical tungsten transport on the detailed 3D structure of the pedestal magnetic field because of the large collisionality of tungsten $\nu^\star \sim 0.1$ (see Figs. 10 and 12), a similar result to that in the ripple cases. No direct effect of RMP or ripple magnetic field structures can thus be seen in tungsten neoclassical transport up to $x \lesssim 0.98$. On the other hand, the smaller collisionalities of the main ion species make them very sensitive to the precise field perturbation and, as a result, neoclassical fluxes of deuterium and tritium with RMP fields differ significantly from the axisymmetric case (and with toroidal field ripple as well), as can be seen comparing Figs. 16 and 11. In order to calculate the ambipolar electric field with RMP fields, the resolution of the simulations has been increased to $N_{theta} = 161$, $N_{zeta} = 12$, $N_{xi} = 80$ and $N_x = 8$ to be ensure that the main species of the plasma, which are less collisional, are properly described. As in the ripple studies, the tungsten flux is neglected when calculating the ambipolar electric field since its concentration is very low. The simulated main species fluxes are shown in Fig. 17 for several radial positions. Notice how results on $x = 0.98$ shown in Fig. 16 and Fig. 17 are virtually identical, expect for the different $E_r$ range. A new effect, that was not present in the studies carried out for 3D equilibria with ripple, is the appearance of extra solutions of the ambipolar condition. To have a clearer view

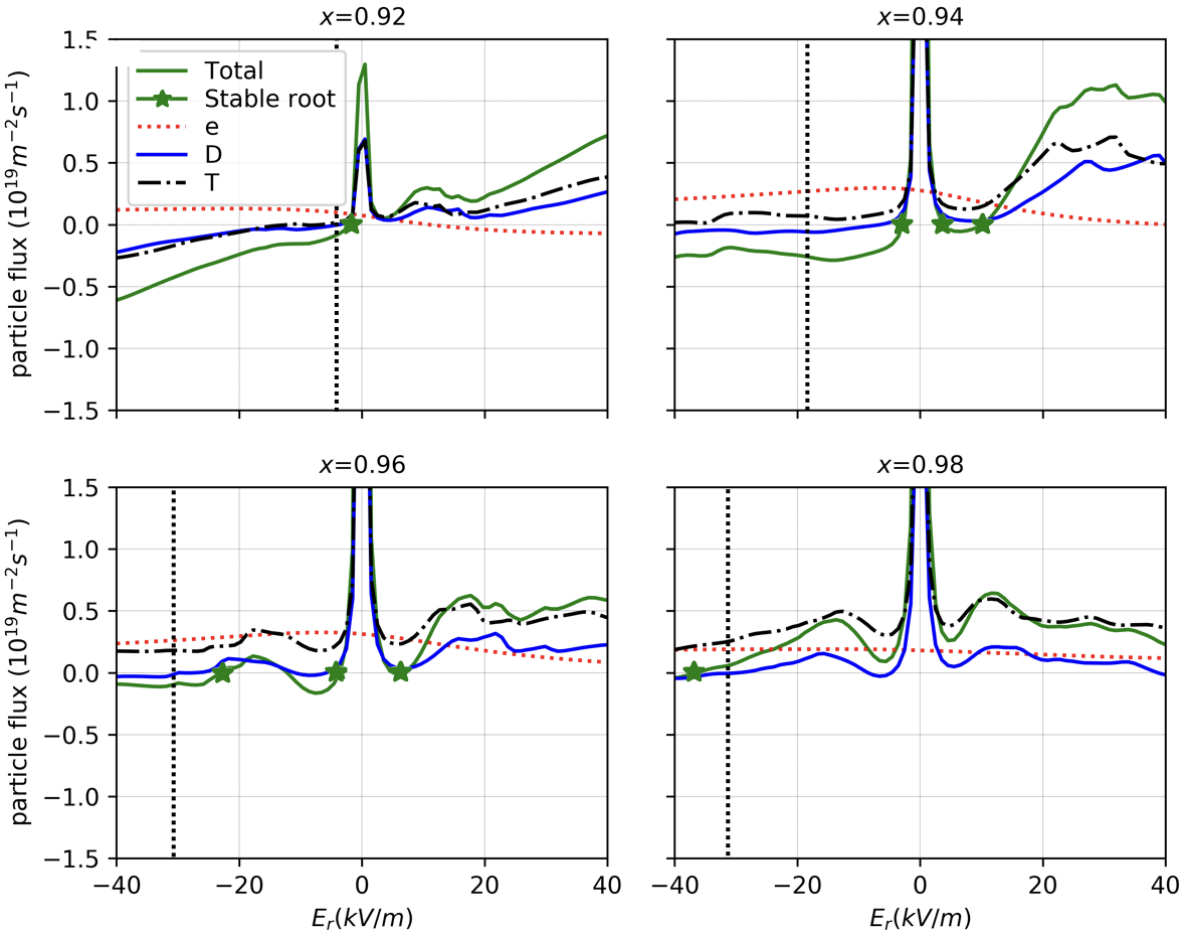


**Figure 17.** Particle fluxes of the different species, except tungsten, versus the radial electric field $E_r$ at four positions within the pedestal region, $x = 0.92$, 0.94, 0.96 and 0.98. The positions of $E_r$ stable roots are marked with a star. The theoretically expected axisymmetric electric field (see Eq. 12) is represented with a vertical dotted line.

of this phenomenology, the electric field root landscape has been represented in Fig. 18, where stable and unstable branches are clearly visible and the value of the field in this branches has been compared with the axisymmetric theoretical electric field. Whereas there is only one (stable) root for $x \lesssim 0.935$, for $x \geq 0.935$ three roots (two stable and one unstable in the middle), five roots (three stable and two unstable) or even seven roots (four stable and three unstable) can be found. Thus, the ambipolar electric field profile is not uniquely defined for the case of RMP fields in ITER. This is well known in the stellarator community where, in the case of three roots, usually the (stable) negative one is named the *ion root* and the (stable) positive one the *electron root* [50]. The complex structure of the fluxes of the main species with RMP fields in ITER suggest the existence of resonances in the Plateau diffusion coefficient, that are sketched on Fig. 19. The base slope (in red) of the plasma flux is associated with the linear $E_r$ term on $A_1$ of Eq. 15; on top of this flux the resonances are added up along with the large non-axisymmetric

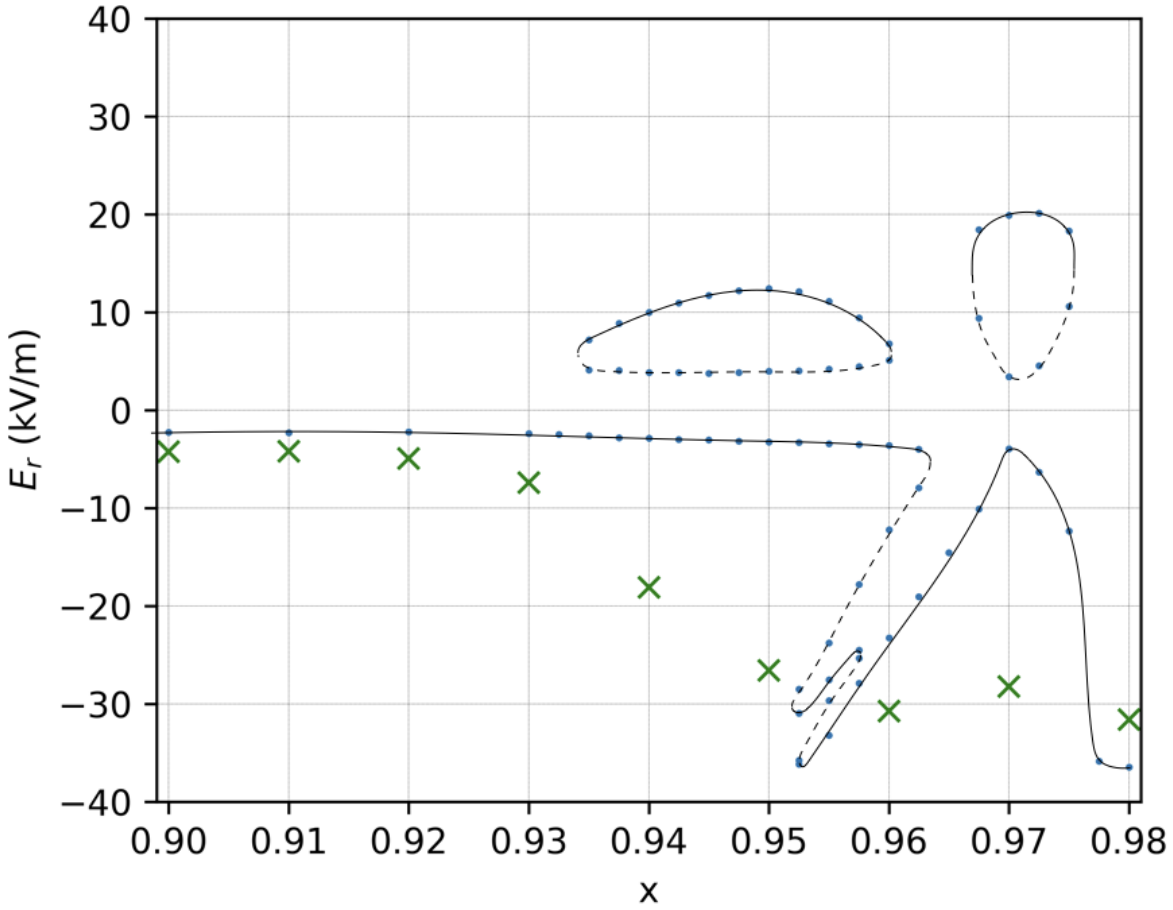


**Figure 18.** Root diagram of the ambipolar radial electric field showing the stable branches (solid dark), unstable branches (dotted branches) and theoretical axisymmetric electric field (crosses).

diffusion at low collisionality for $E_r = 0$ that dominates in the case of RMP fields (see Fig. 10). The stable roots found for the electric field are most of the times less negative than the theoretical electric field obtained in axisymmetric conditions by force balance, which is marked with crosses in Fig. 18. This is in agreement with experiments in which RMP fields are applied that find a less deep electric field well compared to conditions with no RMP fields (see for example [9]).

When several stable solutions of the ambipolar condition are possible, it is necessary to find a criterion to select the one more likely to be realized in the experiment. Based on thermodynamical arguments, the radial electric field should correspond to the solution that minimizes the generalized heat production rate [51]. Thus, a local criteria for selecting a radial electric field root is obtained by choosing the solution which minimizes the dissipation of plasma rotational energy [52, 53]. Since a root that implies a steep radial electric field gradient will produce a strong shear on the poloidal/toroidal velocities and would cause strong dissipation, the criteria used here is

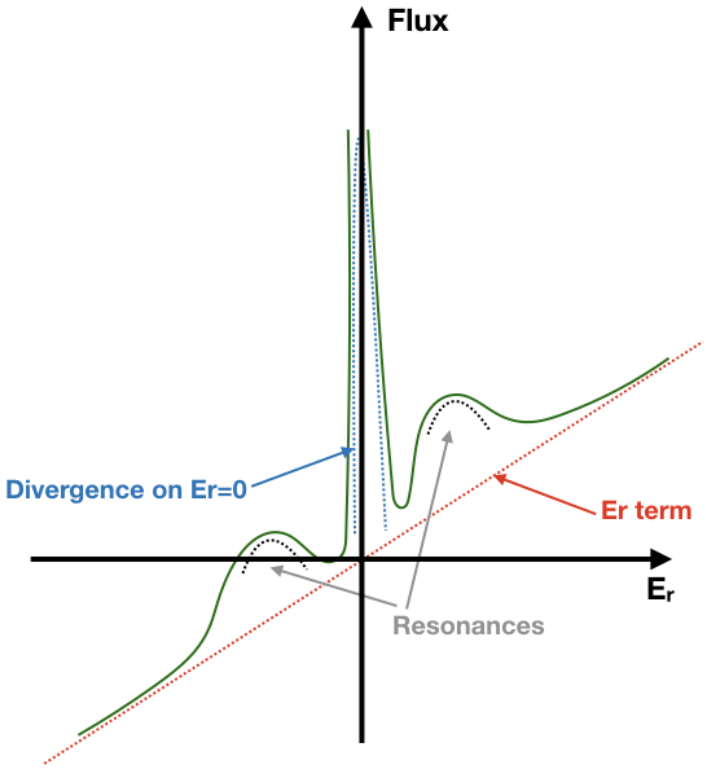


**Figure 19.** Sketch of the particle fluxes of ion species versus the electric field in Fig. 17.

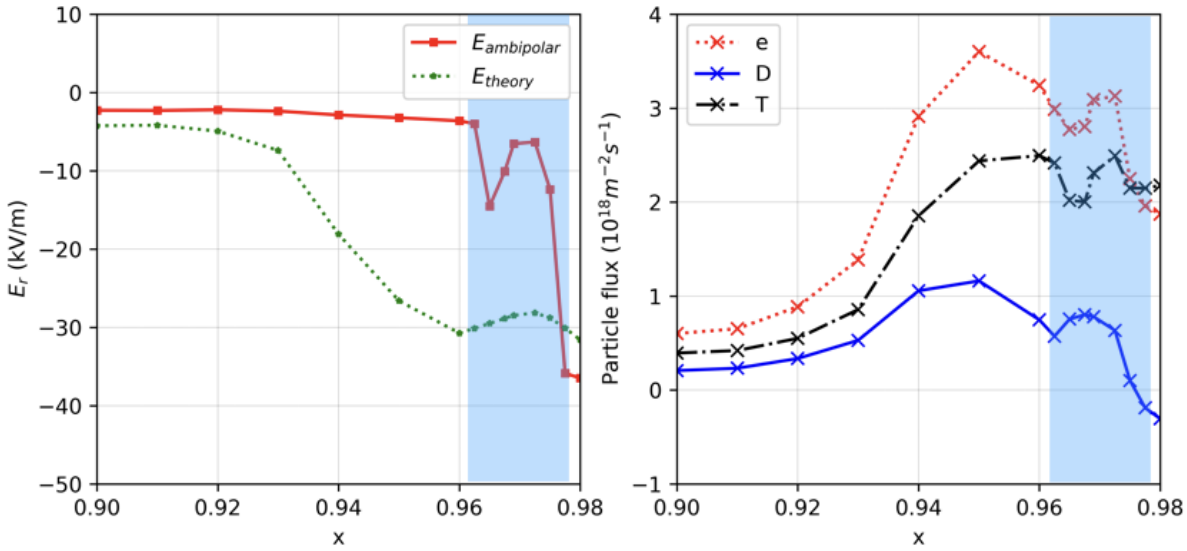


**Figure 20.** Ambipolar electric field $E_r$ (left) and particle fluxes (right) for the selected root. The blue shaded band indicates the region where the chosen solution for the ambipolar electric field shows strong shear.

to choose the root that reproduces the theoretical electric axisymmetric field deep inside the plasma, where the magnetic field is axisymmetric, and minimizes the discontinuities

in the ambipolar radial electric field profile in the pedestal. Following this basic physics criterion a solution without discontinuities is found up to $x \lesssim 0.965$ (largest branch in Fig. 18). For $0.965 \lesssim x < 0.98$ the most reasonable root selection without discontinuities is the negative one. The resulting ambipolar electric field, represented on the left plot of Fig. 20, shows a discontinuity and strong shear around $x \approx 0.97$ (blue shaded on the plot). The fast radial variation of the electric field makes the local approximation used by SFINCS to be questionable and no firm conclusions can be drawn from the results in this outer part of the pedestal. In the rest of the pedestal region ($0.9 < x < 0.965$), the ambipolar electric field associated with this root selection criterion is much smaller than the theoretical axisymmetric field. This reduction is much larger than the one seen in experiments with RMP fields and further studies are in progress to understand if this is the result of ITER specific plasma conditions or due to differences between the real situation (3-D plasma equilibria with closed surfaces and islands and ergodic regions in the outer part of the pedestal) versus the modeled one (closed flux surfaces throughout the pedestal). On the other hand, the shrinking of the electric radial field well in the pedestal, identified with this criterion for root selection, is a common experimental finding in many tokamaks where RMP fields are applied to H-mode plasmas for ELM control [11]. A direct consequence of the strongly reduced ambipolar field is a modification of the particle fluxes, shown also in the right plot of Fig 20. Note the strong impact of the RMP fields on the flux values when compared with the axisymmetric case of Fig. 14 that even reverses the deuterium flux direction. Regarding tungsten transport effects of the RMP fields, the ambipolar electric field for $r < 0.965$ is small enough to reliably calculate the particle flux with SFINCS within the small poloidal Mach number approximation. However, for $r > 0.965$ no clear conclusions can be drawn for tungsten, because SFINCS local approximation is not applicable (besides the issue related to the large electric field value and the poloidal Mach number being large). The calculated tungsten flux as a function of the electric field (Fig. 14) turns out to be very close to the axisymmetric case (Fig. 11) in the full pedestal region, because of the tungsten high collisionality. However, it is essential to understand that the tungsten flux depend on the value of the ambipolar electric field, which is strongly affected by the RMP coils perturbation. Interestingly, because the ambipolar electric field on the inner region of the pedestal is found to be small, the first order neoclassical theory would apply and the effect of the electric field on the particle fluxes can be neglected, being the results of [2] relevant. However, the tungsten flux could be affected for $r > 0.965$, where the electric field may not be small. But no more precise conclusions can be obtained without an accurate expression for the flux under high poloidal Mach number conditions. Note also that other sources of momentum, e.g. those associated with wall friction, might substantially change the radial electric field profile at the edge. These effects, probably require a radially non-local dynamics description and a full radial dissipation minimization and are out of the scope of this work. Based on the neoclassical calculations presented here, RMP fields in ITER are expected to strongly affect the ambipolar radial electric field for any of the choices of

the roots, with a clear tendency toward less negative, or even positive, values at the pedestal.

Finally, it is important to note that all the calculations presented here were done keeping fixed all radial profiles, i.e.; without recalculating the 3D MHD equilibria and the plasma profiles to account for transport changes at the edge. The consequences of the neoclassical pedestal transport modification due to ripple RMP perturbations on the main plasma require a self-consistent treatment including both transport and sources (chiefly high field side pellet injection in ITER) which is out of the scope of this work.

## 7. Conclusions

In this work we have modelled detailed 3-D MHD plasma equilibria for the reference ITER Q = 10 baseline scenario plasma and evaluated the consequences of the 3-D field features on the ambipolar electric field and neoclassical transport in the pedestal region with the SFINCS code. Two types of 3-D plasma equilibria have been considered: one corresponding to the ripple of the toroidal field, due to the finite number of toroidal field coils and the other to RMP fields resulting from the application of ELM control coils in ITER.

Different benchmarks have been performed to compare the SFINCS results against reference neoclassical transport modelling codes both for axisymmetric (NEO and NCLASS) and non-axisymmetric (MOCA) equilibria, finding excellent agreement for low electric field values. For axisymmetric equilibria with the nominal value of the electric field from force balance considerations, it is found that the poloidal Mach number of tungsten in the ITER pedestal plasma is not small and this renders the usual first order evaluation of neoclassical transport questionable. Second order terms, included partially in SFINCS, suggest that the effects associated with the high poloidal number of tungsten in the pedestal could have significant impact on neoclassical transport and could even change the direction of its flow compared to conventional axisymmetric simulations.

The direct effect of the toroidal field ripple on tungsten pedestal transport in ITER, for a fixed electric field profile, is found to be negligible. The reason being the high collisionality of tungsten impurities within the pedestal region ($\nu^\star \sim 0.1$), which are not collisionless enough to *feel* the effect of the non-axisymmetric field structures. On the other hand, clear effects can be seen in the transport of the main species, which for ripple values larger than 1% even reverse the direction of the deuterium flux for $Q = 10$ plasmas. Interestingly, the ambipolar field does not show such sensitivity, since ripple values around 2% are necessary to modify the $E_r$ profile. The conclusion is, thus, that for the expected ripple of ITER 15MA/5.3T, which includes ferromagnetic inserts to reduce the ripple to around 0.3%, axisymmetric calculations of the neoclassical transport of the main species and tungsten should be appropriate (with the caveat above regarding the accuracy of these modeling results in view of the high poloidal Mach number). An assessment of these effects for H-mode plasmas to be explored in advance of $Q = 10$ operation with lower toroidal field and larger ripple values (0.55% - 1.3%)

will be performed to determine if this result applies to all ITER H-modes or only to those at 5.3T.

For RMP fields, the edge structure of the 3-D equilibria is significant enough to cause the appearance of several solutions for the ambipolar condition. This leads to several $E_r$ roots of the electric field, which may be of importance in the context of the achievement of ELM suppression for which $\omega_\perp \approx 0$ at the pedestal is required [54, 55] and will be the subject of future studies. Throughout most of the pedestal plasma, it is found that the ambipolar field is less negative than that for the axisymmetric equilibrium. Large negative electric fields remain only in the exterior part of the pedestal. The decrease in magnitude of the electric field and the shrinking of the region with larger negative field in the pedestal when RMP fields are applied are in qualitative agreement with experimental observations. The change in the field leads to an increase of the radial plasma flux (both for electrons and ions). This is in qualitative agreement with the experimental findings (density pump-out) when RMP fields are applied and does not require the formation of ergodic surfaces in the plasma. Some of the stable branches found, but not those with lowest rotational energy dissipation, can even induce a reversal of the electric field sign. The changes to the electric field with RMP fields at the pedestal modify the neoclassical flux of main (deuterium and tritium) ions compared to the axisymmetric case but much less that of tungsten. The direct effect of RMP fields on tungsten transport are small due, again, to its high collisionality. Throughout most of the pedestal plasma, where the electric field values are low, tungsten neoclassical transport is similar to that obtained in axisymmetric studies for ITER. For the narrow region with large electric fields, it is not possible to extract robust conclusions due to, first, the possible radially non-local character of the dynamics and, second, the issues related to the accuracy of neoclassical transport with the high poloidal Mach number for tungsten.

A more detailed analysis of electric field resonances for ITER plasma equilibria with a wider range of RMP fields (magnitude of ELM control current and alignment of the applied field with the plasma field) and a more refined study of the thermodynamically preferred roots for the electric field at the pedestal will be carried out in future studies. Further theoretical and computational developments are required for an accurate description of tungsten transport at the ITER pedestal with large poloidal flows and RMP fields and also including the self-consistent effect of this transport on the plasma MHD equilibria and species profiles.

## 8. Acknowledgments

This work has been carried out within the work programme of the ITER Scientist Fellow Network. The authors would like to thank C.D. Beidler, M. Landreman and E.A. Belli for useful comments. This research has been partially sponsored by the project SIMTURB-CM-UC3M from the Convenio Plurianual Comunidad de Madrid-Universidad Carlos III de Madrid and by Spanish National Research Project No.

ENE2015-68265. Use have also been made of *Uranus*, a supercomputer cluster located at Universidad Carlos III de Madrid (Spain) funded jointly by EU FEDER funds and by the Spanish Government via the National Research Project Nos. UNC313- 4E-2361, ENE2009-12213-C03-03, ENE2012-33219, and ENE2012-31753.

Disclaimer: ITER is the Nuclear Facility INB no. 174. The views and opinions expressed herein do not necessarily reflect those of the ITER Organization.

## References

[1] SNYDER, P., GROEBNER, R., HUGHES, J., et al., Nuclear Fusion **51** (2011) 103016.
[2] DUX, R., LOARTE, A., FABLE, E., and KUKUSHKIN, A., Plasma Physics and Controlled Fusion **56** (2014) 124003.
[3] WESSON, J., *Tokamaks*, Oxford University Press, New York, 3rd edition, 2004.
[4] LAMZIN, E. A., AMOSKOV, V. M., GAPIONOK, E. I., et al., IEEE Transactions on Applied Superconductivity **22** (2012) 4901004.
[5] LOARTE, A., SAIBENE, G., SARTORI, R., et al., Nuclear Fusion **45** (2003) 1549.
[6] GIANCARLI, L. M., AHN, M. Y., BONNETT, I., et al., Fusion Engineering and Design **136** (2018) 815.
[7] ROCCELLA, M., LUCCA, F., ROCCELLA, R., et al., Fusion Engineering and Design **82** (2007) 709.
[8] PÜTTERICH, T., DUX, R., JANZER, M., and MCDERMOTT, R., Journal of Nuclear Materials **415** (2011) S334.
[9] COENEN, J. W., SCHMITZ, O., UNTERBERG, B., et al., Nuclear Fusion **51** (2011) 063030.
[10] EVANS, T. E., MOYER, R. A., THOMAS, P. R., et al., Physical Review Letters **92** (2004) 235003.
[11] NAZIKIAN, R., PAZ-SOLDAN, C., CALLEN, J. D., et al., Physical Review Letters **114** (2015) 105002.
[12] LI, L., LIU, Y. Q., LOARTE, A., et al., Nuclear Fusion **59** (2019) 096038.
[13] HIRSHMAN, S. P. and WHITSON, J. C., Physics of Fluids **26** (1983) 3553.
[14] HIRSHMAN, S. P., VAN RIJ, W. I., and MERKEL, P., Computer Physics Communications **43** (1986) 143.
[15] SANCHEZ, R., HIRSHMAN, S. P., WHITSON, J. C., and WARE, A. S., Journal of Computational Physics **161** (2000) 576.
[16] GALEEV, A. A. and SAGDEEV, R. Z., Sov. Phys. JETP **26** (1968) 233.
[17] ROSENBLUTH, M. N., HAZELTINE, R. D., and HINTON, F. L., Physics of Fluids **15** (1972) 116.
[18] BEIDLER, C. D., ALLMAIER, K., ISAEV, M. Y., et al., Nuclear Fusion **51** (2011) 076001.
[19] HELANDER, P. and SIMAKOV, A. N., Physical Review Letters **101** (2008) 145003.
[20] MAASSBERG, H., BEIDLER, C. D., and TURKIN, Y., Physics of Plasmas **16** (2009) 072504.
[21] LANDREMAN, M. and ERNST, D. R., Journal of Computational Physics **243** (2013) 130.
[22] LANDREMAN, M., SMITH, H. M., MOLLÉN, A., and HELANDER, P., Physics of Plasmas **21** (2014) 042503.
[23] DINKLAGE, A., BEIDLER, C. D., HELANDER, P., et al., Nature Physics **14** (2018) 855.
[24] PAUL, E. J., LANDREMAN, M., POLI, F. M., et al., Nuclear Fusion **57** (2017) 116044.
[25] SHIMADA, M., CAMPBELL, D. J., MUKHOVATOV, V., et al., Nuclear Fusion **47** (2007) S1.
[26] POLEVOI, A., LOARTE, A., DUX, R., et al., Nuclear Fusion **58** (2018) 056020.
[27] POLEVOI, A., LOARTE, A., KUKUSHKIN, A. S., et al., Nuclear Fusion **57** (2017) 022014.
[28] PÜETTERICH, T., NEU, R., DUX, R., et al., Plasma Physics and Controlled Fusion **50** (2008) 085016.

[29] MITCHELL, N., DEVRED, A., LIBEYRE, P., LIM, B., and SAVARY, F., IEEE Transactions on Applied Superconductivity **22** (2012) 4200809.
[30] LIU, Y., HAM, C. J., KIRK, A., et al., Plasma Physics and Controlled Fusion **58** (2016) 114005.
[31] EVANS, T. E., ORLOV, D. M., WINGEN, A., et al., Nuclear Fusion **53** (2013) 093029.
[32] BELLI, E. and CANDY, J., Plasma Physics and Controlled Fusion **50** (2008).
[33] HOULBERG, W. A., SHAING, K. C., HIRSHMAN, S. P., and ZARNSTORFF, M. C., Physics of Plasmas **4** (1997) 3230.
[34] TRIBALDOS, V., Physics of Plasmas **8** (2001) 1229.
[35] TRIBALDOS, V. and GUASP, J., Plasma Physics and Controlled Fusion **47** (2005) 545.
[36] HELANDER, P. and SIGMAR, D. J., *Collisional transport in magnetized plasmas*, volume 4 of *Cambridge monographs on plasma physics*, Cambridge University Press, 2002.
[37] ANGIONY, C. and HELANDER, P., Plasma Physics and Controlled Fusion **56** (2014) 124001.
[38] GARCIA-REGAÑA, J. M., BEIDLER, C. D., KLEIBER, R., et al., Nuclear Fusion **57** (2017) 056004.
[39] CASSON, F., ANGIONI, C., BELLI, E., et al., Plasma Physics and Controlled Fusion **57** (2015) 014031.
[40] LANDREMAN, M. and ERNST, D., Plasma Physics and Controlled Fusion **54** (2012) 115006.
[41] BELLI, E. A. and CANDY, J., Plasma Physics and Controlled Fusion **57** (2015) 054012.
[42] A.LOARTE, HOSOKAWA, M., POLEVOI, A., et al., Evaluation of tungsten transport and concentration control in iter scenarios, in *26th IAEA Fusion Energy Conference, Kyoto*, pp. PPC/2–1, 2016.
[43] BELLI, E. A., CANDY, J., and ANGIONI, C., Plasma Physics and Controlled Fusion **56** (2014) 124002.
[44] HINTON, F. L. and WONG, S. K., Physics of Fluids **28** (1985) 3082.
[45] VIEZZER, E., PÜTTERICH, T., ANGIONI, C., et al., Nuclear Fusion **54** (2014) 012003.
[46] BEIDLER, C. D., ISAEV, M. Y., KASILOV, S. V., et al., ICNTS - Impact of Incompressible E x B Flow in Estimating Mono-Energetic Transport Coefficients, in MORISAKI, T., editor, *Proceedings of 17th International Toki Conference and 16th International Stellarator and Heliotron Workshop, Toki*, 2007.
[47] HIRSHMAN, S. P., SHAING, K. C., VAN RIJ, W. I., BEASLEY, C. O. J., and CRUME, E. C. J., Physics of Fluids **29** (1986) 2951.
[48] BOOK, D. L., NRL Plasma Formulary, Naval research Laboratory, Washington, DC, 1990.
[49] BOOZER, A. H. and KUO-PETRAVIC, G., Physics of Fluids **24** (1981) 851.
[50] YOKOYAMA, M., MAASSBERG, H., BEIDLER, C. D., et al., Nuclear Fusion **47** (2007) 1213.
[51] SHAING, K., Physics of Fluids **27** (1984) 1567.
[52] MAASSBERG, H., BURHENN, R., GASPARINO, U., et al., Physics of Fluids B **5** (1993) 3627.
[53] MAASSBERG, H., BEIDLER, C. D., GASPARINO, U., et al., Physics of Plasmas **7** (2000) 295.
[54] SUTTROP, W., KIRK, A., BOBKOV, V., et al., Nuclear Fusion **58** (2018) 096031.
[55] PAZ-SOLDAN, C., NAZIKIAN, R., CUI, L., et al., Nuclear Fusion **59** (2019) 056012.